Title:

Retinal stem cells modulate proliferative parameters to coordinate post-embryonic morphogenesis in the eye of fish

Authors:

Erika Tsingos[1,*], Burkhard Höckendorf[1†], Thomas Sütterlin[2], Stephan Kirchmaier[1,‡], Niels Grabe[2], Lázaro Centanin[1], Joachim Wittbrodt[1,*]

Affiliations:

[1]Centre for Organismal Studies Heidelberg, Heidelberg University.

[2]National Center for Tumor Diseases, Hamamatsu TIGA Center, Bioquant, Heidelberg University.

[*]Correspondence to: erika.tsingos@cos.uni-heidelberg.de, jochen.wittbrodt@cos.uni-heidelberg.de.

[†] Present address: Howard Hughes Medical Institute, Janelia Research Campus.

[‡] Present address: Deutsches Krebsforschungszentrum Heidelberg

Impact statement:

3D niche topology imposes a spatially biased random stem cell loss, which is differentially fine-tuned in neural retina and retinal pigmented epithelium to regulate growth, shape, and cellular topology.

Abstract:

Combining clonal analysis with a computational agent based model, we investigate how tissue-specific stem cells for neural retina (NR) and retinal pigmented epithelium (RPE) of the teleost medaka (*Oryzias latipes*) coordinate their growth rates. NR cell division timing is less variable, consistent with an upstream role as growth inducer. RPE cells divide with greater variability, consistent with a downstream role responding to inductive signals. Strikingly, the arrangement of the retinal ciliary marginal zone niche results in a spatially biased random lineage loss, where stem- and progenitor cell domains emerge spontaneously. Further, our data indicate that NR cells orient division axes to regulate organ shape and retinal topology. We highlight an unappreciated mechanism for growth coordination, where one tissue integrates cues to synchronize growth of nearby tissues. This strategy may enable evolution to modulate cell proliferation parameters in one tissue to adapt whole-organ morphogenesis in a complex vertebrate organ.

Main Text:

Introduction

To maintain proper proportions, growth must be regulated at the level of the whole body, the size of each organ, and the size of tissues within an organ (Roselló-Díez and Joyner, 2015). Some regulatory mechanisms are shared, while others are specific to each level or to particular organs (Lui and Baron, 2011; Roselló-Díez and Joyner, 2015). Systemic signals couple nutrition to growth to coordinate growth of all organs at the organismal level (Buchmann *et al.*, 2014; Droujinine and Perrimon, 2016). In addition to extrinsic systemic factors, transplantation experiments showed that many organs, including the eye, grow autonomously according to intrinsic factors (Wallman and Winawer, 2004; Roselló-Díez and Joyner, 2015). Growth coordination mechanisms have been studied at the level of the whole organism and inter-organ communication (Buchmann *et al.*, 2014; Droujinine and Perrimon, 2016), but feedback mechanisms between constituent tissues of an organ remain largely unexplored both experimentally and at a conceptual level (Buchmann *et al.*, 2014).

Teleost fish grow throughout their lives, increasing massively in size (Johns and Easter, 1977). The teleost medaka (*Oryzias latipes*) grows roughly ten-fold from hatching to sexual maturity within 2-3 months (Figure 1-figure supplement 1 A). Unlike embryonic morphogenesis, during post-embryonic growth all organs must scale with the increasing body size while fully functioning. In the eye, continuous growth must be additionally balanced with continuous shape-keeping: Proper optics, and thus vision, requires a precise 3D shape. Highly visual shallow water fish such as medaka have near-perfect hemispherical eyes (Fernald, 1990; Nishiwaki *et al.*, 1997; Beck *et al.*, 2004). The growth rates of all eye tissues must perfectly match, otherwise the organ would deform, akin to a bimetallic strip. Thus, the eye of fish provides an excellent system to explore how anatomically and functionally distinct tissues coordinate to grow and maintain the shape of an organ in functional homeostasis (Johns and Easter, 1977; Centanin *et al.*, 2014).

The vertebrate eye consists of multiple concentric tissues, including the neural retina (NR) and the retinal pigmented epithelium (RPE) (Figure 1 A). In fish and amphibians, these tissues grow from a ring-shaped stem cell niche in the retinal periphery: the ciliary marginal zone (CMZ) (Johns, 1977; Harris and Perron, 1998; Amato *et al.*, 2004). The CMZ can be subdivided into a peripheral stem- and a central progenitor cell domain; stem cells are believed to have the potential for indefinitely many cell divisions while progenitor cells divide only a handful of times (Raymond *et al.*, 2006; Centanin *et al.*, 2014; Wan *et al.*, 2016; Shi *et al.*, 2017). At the very periphery of the CMZ, about 5 rows of cells express the stem cell marker retina-specific homeobox gene 2 (Rx2) (Reinhardt *et al.*, 2015; Wan *et al.*, 2016;

Tang *et al.*, 2017). The CMZ is a bi-partite niche, with tissue-specific stem cells for NR and RPE (Shi *et al.*, 2017). In medaka, stem cells for NR and RPE are strictly separate, as demonstrated by transplantations at blastula stage and genetic recombination after hatching (Centanin *et al.*, 2011, 2014). Thus, medaka NR and RPE are independently growing tissues with identical topology.

As a population, CMZ cells appositionally add new cells in concentric rings as shown by label incorporation with thymidine analogues (Johns, 1977; Centanin *et al.*, 2011). Individual stem cells labeled by genetic markers form clonal progeny in so-called Arched Continuous Stripes (ArCoS; Figure 1 B) (Centanin *et al.*, 2011, 2014). Medaka NR stem cells produce the full complement of neuronal cells in apico-basal clonal columns (Figure 1- figure supplement 2 A'-B) (Centanin *et al.*, 2011, 2014; Lust and Wittbrodt, 2018). These differentiated retinal cells grow little in size (Johns, 1977), retain their relative position over time (Johns, 1977; Centanin *et al.*, 2011), and have negligible death rates (Johns and Easter, 1977; Stenkamp, 2007). Thus, the only parameter available to NR and RPE to coordinate their growth rates is the proliferation of the tissue-specific CMZ stem cells.

Stem cells have long been defined by an unlimited self-renewal capacity (Watt and Hogan, 2000; Clevers and Watt, 2018). Two general strategies underlie long-term maintenance of stem cells: 1) a deterministic model where every single division produces a stem- and a progenitor daughter cell ("invariant asymmetry"); and 2) a stochastic model where cells divide symmetrically, and the daughter cells have a probability to stay as stem cells or commit to a progenitor fate ("neutral drift") (Watt and Hogan, 2000; Clevers and Watt, 2018). One tenet of this model is neutral competition: Stem cells randomly displace one another, resulting in the "loss" of lineages where all progeny commit to a progenitor fate until the entire niche is occupied by a single clone (Colom and Jones, 2016; Clevers and Watt, 2018).

Strikingly, the medaka retina diverges from the neutral drift model. The CMZ maintains a polyclonal stem cell population for both the NR and the RPE, and in particular NR stem cells undergo asymmetric self-renewing divisions throughout the life of the animal (Centanin *et al.*, 2011, 2014). It remains unclear whether stem cell proliferation in the CMZ follows a purely deterministic model, or whether it follows a strategy in-between invariant asymmetry and neutral drift.

In this work we combine *in vivo* and *in silico* clonal analysis in the NR and RPE of medaka to address how these tissues coordinate their growth rates. We find that RPE stem cells have highly variable cell division timing consistent with a downstream role in the control hierarchy, whereas NR stem cells display less variability consistent with an upstream role in inducing growth in nearby tissues. Our simulation predicts that the spatial segregation of stem and progenitor CMZ domains is an emergent property, as the topology of the retinal niche

103 preconditions the retina to a spatially biased neutral drift. NR stem cells deviate from a purely
104 random drift model by preferential division axis orientation and differential modulation of
105 division parameters along the CMZ circumference. We propose that during post-embryonic
106 growth of the teleost eye, the NR CMZ forms a hub for integrating external and internal
107 stimuli that affect cell division parameters, which ultimately direct the growth and shape of
108 the entire eye.

Results

Clonal analysis indicates NR and RPE follow different post-embryonic growth modes

Retinal cells follow an exquisite spatiotemporal order (Figure 1 B-C, Figure 1-figure supplement 1 B). Thus, clones derived from stem cells are a frozen record of past cell divisions (Centanin *et al.*, 2011, 2014), offering a window of opportunity to study stem cell properties in the NR and RPE.

We experimentally generated NR ArCoS by randomly labelling individual NR stem cells using the Rx2::^{ERT2}Cre, Gaudí$^{2.1}$ line in hatchling medaka, and analyzing the eyes in adult fish as previously described (Centanin *et al.*, 2014; Reinhardt *et al.*, 2015). The Rx2 promoter drives the inducible Cre recombinase in stem cells at the very periphery of the CMZ (Reinhardt *et al.*, 2015). A recombined stem cell generates a stripe of GFP-positive progeny in an otherwise GFP-negative retina (Centanin *et al.*, 2014). In proximal view, NR ArCoS emanated as rays from the central embryonic retina, the part of the eye that was already differentiated at the timepoint of Cre-mediated recombination (Figure 1 D).

We visualized RPE ArCoS by mosaic knockout of pigmentation using CRISPR/Cas9 targeted to the gene oculo-cutaneous albinism 2 (Oca2), which is required for melanosome maturation (Fukamachi *et al.*, 2004; Lischik *et al.*, 2018). RPE stem cells with a bi-allelic mutation in Oca2 generate unpigmented stripes, analogous to RPE ArCoS obtained by transplantation (Centanin *et al.*, 2011). RPE ArCoS frequently branched, forming irregular stripes variable in size and shape (Figure 1 E). These qualitative differences in clonal pattern suggested that despite their identical topology, the division behavior of NR and RPE stem cells differed.

A 3D agent-based model of retinal tissues

Clonal data generates a distribution of outcomes that is challenging to analyse and easy to misinterpret (Klein *et al.*, 2007). The curved retinal surface and spatial extent of the niche pose a further challenge. We overcome these challenges by comparing experimental clonal data with simulated clonal data from a 3D agent based cell-centered overlapping spheres model built in the platform EPISIM (Sütterlin *et al.*, 2013, 2017, 2019). This modelling technique represents cells as discrete objects (*e.g.* spheres) that physically interact through forces acting on the cell centers; the spheres are allowed to slightly overlap to simulate cell deformability and allow a tight cell packing (Sütterlin *et al.*, 2013, 2017). This level of abstraction is ideally suited to the tightly packed pseudocrystalline mosaic of retinal cells (Johns, 1981; Nishiwaki *et al.*, 1997; Perez-Saturnino *et al.*, 2018), and has been used previously to model clonal data in skin and gut epithelia (Osborne *et al.*, 2010; Buske *et al.*, 2011; Li *et al.*, 2013).

Our retinal tissue model consists of a layer of spheres (representing either NR or RPE cells) on a hemisphere (representing the rest of the organ that is not explicitly modelled; Figure 2 A). The RPE is a monolayer, thus each model cell corresponds to one RPE cell. In the NR, CMZ stem cells form a monolayer, and their differentiated progeny arrange in multiple neuronal layers (Johns, 1977; Raymond *et al.*, 2006). We observed that clonal progeny of CMZ stem cells retained close proximity with little spread tangential to the retinal surface, forming clonally related "columns" (Figure 1 Supplement 2 A'-B) (Centanin *et al.*, 2011, 2014; Lust and Wittbrodt, 2018). We took advantage of this fact to abstract each differentiated clonal column as a single cell in the simulation.

In vivo, the spatial extent of the CMZ stem cell domain is believed to be defined by cues such as nearby blood vessels (Wan *et al.*, 2016; Tang *et al.*, 2017). Therefore, we defined the virtual stem cell domain with a fixed size of 25 µm, *i.e.* 5 rows of cells, reflecting the endogenous scale of the Rx2-expressing CMZ domain (Reinhardt *et al.*, 2015; Wan *et al.*, 2016; Tang *et al.*, 2017). *In vivo*, NR stem cells divide predominantly asymmetrically, but also undergo symmetric divisions (Centanin *et al.*, 2014). The rates of asymmetric and symmetric divisions are unknown; likewise, it is unknown whether these rates are deterministically defined or an emergent property of an underlying stochastic system. Since stochastic cell divisions successfully describe the proliferation of committed retinal progenitor cells in larval zebrafish (Wan *et al.*, 2016), we used a simple stochastic mechanism for our initial model. Virtual stem cells commit to divide with a fixed probability $p_{\mathrm{div}} = \frac{1}{26}\mathrm{h}^{-1}$ and intervals between subsequent cell divisions must fulfill a minimum cell cycle length $t_{\mathrm{cellCycle}} = 24\mathrm{h}$. These values lie within a biologically plausible range estimated from experimentally measured growth rates and a parameter scan of the simulation (Appendix 1 section 3.3). All divisions are symmetric, resulting in two stem cells; cells differentiate and stop cycling when they exit the virtual CMZ after being pushed out by cellular crowding.

To prevent physically implausible cell crowding, cell-center based models include a density-dependent inhibition of cell division (Pathmanathan *et al.*, 2009; Osborne *et al.*, 2017; Sütterlin *et al.*, 2017). In our model, inhibition occurs in cells whose average overlap with all neighbors exceeds a fraction of the cell's diameter given by the model parameter $\delta_{\mathrm{ol\_threshold}}$ (Figure 2-figure supplement 1; Appendix 1, section 2.4). Based on *in vivo* observations (Lyall, 1957; Johns, 1977; Ohki and Aoki, 1985), the growing virtual eye gradually moves cells apart as it expands, thus decreasing cell density (Figure 2-figure supplement 2; Appendix 1 section 2.2). Continuous proliferation in the CMZ counteracts this decrease *in vivo* (Johns, 1977; Johns and Easter, 1977); likewise, the ever-increasing virtual cell population optimally fills the hemisphere at all times (Video 1; Video 2). Our model distills the complexity of the

system and replicates the exquisite spatiotemporal growth order observed *in vivo* (Figure 2 B', B'').

Fundamental feedback modes of organ and cell growth impact on clonal patterns

Conceptually, we reasoned that feedback between tissues in an organ can be wired in two fundamental ways: Either the tissue of interest acts upstream to induce growth of other tissues (Figure 2 C'; "inducer growth mode"), or, vice versa, the tissue of interest lies downstream of growth cues from another tissue in the organ (Figure 2 D'; "responder growth mode"). Possible biological mechanisms for these growth modes could be mechanical, biochemical, or a combination of both. For example, in the inducer growth mode cells could instruct organ growth by modifying the extracellular matrix or by paracrine signalling (Buchmann *et al.*, 2014; Droujinine and Perrimon, 2016). These stimuli instruct tissues with the responder growth mode to grow, *e.g.* by alleviating contact inhibition or by providing permissive proliferation signals (Buchmann *et al.*, 2014; Droujinine and Perrimon, 2016). In an organ composed of multiple tissues, one tissue may be the driver for growth, while the rest follows.

We examined how these two conceptual growth modes affected stem cell dynamics in the simulation. In our implementation of the inducer growth mode, an increase in cell number induces growth of the virtual eye's radius (Appendix 1-equation 5). Implicit in this growth mode is the assumption that cell division is not inhibited by the degree of cell crowding normally present in the tissue (otherwise the organ would never grow). Therefore, we set the tolerated overlap threshold $\delta_{\text{ol\_threshold}} = 0.4$, a value which we determined by parameter scan to minimize cell division inhibition while preventing physically implausible crowding (Appendix 1 Text, section 3.2).

In the responder growth mode, we let the radius grow linearly over time (Appendix 1-equation 6). In this growth mode, cells must stop dividing until they receive an external stimulus. We take advantage of the pre-existing local density sensing to implement a physical stimulus akin to contact inhibition. Thus, we set the tolerated overlap threshold $\delta_{\text{ol\_threshold}} = 0.2$ to maximize cell division inhibition at homeostatic density (Appendix 1, section 3.2). As growth of the hemisphere decreases cell density, cells dynamically respond to growth of the eye by resuming divisions.

In short, the growth modes in our simulation differ only in: 1) the growth equation for the radius of the hemisphere, 2) the value of the threshold parameter $\delta_{\text{ol\_threshold}}$ where local cell density inhibits cell divisions (for details, the reader is referred to Appendix 1, sections 2.3; 2.4; and 3.2).

We obtained virtual ArCoS regardless of growth mode (Figure 2 C'', D''). The growth mode strongly impacted on the shape of ArCoS. Clones in the inducer growth mode formed well-confined stripes with low variation in shape (Figure 2 C'''). In the responder growth mode, the virtual clones frequently intermingled and broke up into smaller clusters (Figure 2 D'''). Specifically, the growth modes impacted on variation in cell division timing (Figure 2 C'''', D''''). In the responder growth mode, local competition for space increased cell division intervals, particularly among cells exceeding the tolerated overlap threshold $\delta_{\mathrm{ol\_threshold}} = 0.2$ (Figure 2 D''''). Thus, the model predicted distinct levels of variation in cell division timing in retinal tissues following the inducer or responder growth modes.

NR stem cells have less variable cell division timing compared to the RPE

Since the position of cells in the retina reflects their birth order (Centanin *et al.*, 2011, 2014), we reasoned that in the extreme case of no variation in cell division timing, each clone forms a continuous, unbranching stripe (Figure 3 B, left). In the opposite highly variable case, clones frequently branch or merge into polyclones, as well as fragment into several small patches (Figure 3 B, right). Thus, with increasing variation in cell division timing, we expect an increasing variation in clone width, and an increasing incidence of clone branching and fragmentation.

To quantitatively underpin our previous observations, we compared simulated clones of the inducer and responder growth modes to clones in the NR and RPE (Figure 3 A', A''). We circumvented biases associated with fusion and fragmentation of clones by analyzing "patches", *i.e.* contiguous domains of segmented pixels. A patch may entail a (sub-)clone, or multiple clones (*i.e.* a polyclone) (Figure 3-figure supplement 1; Video 3). To assay our experimental and simulated data, we unrolled the retina with a coordinate transform (Figure 3-figure supplement 2 C) and quantified three different metrics: patch width variance, branching, and fragmentation.

To assay patch width variance, we aligned and superimposed all patches (Figure 3 C', C''), and quantified the distribution of maximum patch width (Figure 3-figure supplement 2 A; Figure 3-source data 7). Confirming our previous qualitative observations, NR patches formed a narrow stripe, while the width of RPE patches showed much greater variation (Figure 3 C'; Figure 3-figure supplement 2 A). The variance of NR and RPE patches was significantly different at the 0.05 level ($p = 3.50 \cdot 10^{-12}$, F-test of equality of variance). In striking agreement to the experimental data, simulated patches in the inducer growth mode had low variation in width, while patches in the responder growth mode spread widely (Figure 3 C''; Figure 3-figure supplement 2 A). The variances in the simulated conditions were significantly different at the 0.05 level ($p = 5.84 \cdot 10^{-7}$, F-test of equality of variance), but highly

similar between NR and inducer ($p = 0.56$, F-test of equality of variance); and RPE and responder ($p = 0.21$, F-test of equality of variance).

To measure branching we skeletonized the patches, and quantified the distribution of nodes per patch and condition (Figure 3 D; Figure 3-source data 8). Patches in the NR and in the inducer growth mode were overwhelmingly stripe-like with no branch points (Figure 3 D; inset I), with similar node distribution ($p = 0.64$, Wilcoxon rank sum test). In contrast, both NR and inducer differed significantly at the 0.05 level from the distribution in the RPE and responder growth mode (NR-RPE: $p = 3.93 \cdot 10^{-6}$; NR-responder: $p = 3.26 \cdot 10^{-4}$; inducer-RPE: $p = 6.24 \cdot 10^{-7}$; inducer-responder: $p = 7.00 \cdot 10^{-5}$, Wilcoxon rank sum test). Patches in the RPE and in the responder growth mode frequently bifurcated or merged, creating branching shapes with inclusions indicative of clone intermingling (Figure 3 D; inset III). RPE and responder growth mode were highly similar in this metric ($p = 0.38$, Wilcoxon rank sum test).

Not all patches were contiguous with the embryonic retina. Such “late arising patches” result if a cell divided intermittently with periods of dormancy, leaving clone fragments behind (Figure 3 B, highly variable scenario). We quantified fragmentation by plotting the occurrence of late arising patches along the normalized post-embryonic retinal radius (Figure 3 E; Figure 3-source data 9). In the NR late patches clustered in the central post-embryonic retina and waned thereafter. Thus clone fragments were not equally distributed, consistent with lower levels of cell division variability and a majority of continuous stripe-like clones. In contrast, the RPE displayed an even distribution indicative of frequent fragmentation throughout the life of the animal as predicted for the highly variable scenario (NR-RPE: $p = 1.74 \cdot 10^{-3}$, Wilcoxon rank sum test). The simulated data showed the same tendency, to a lesser degree, as the central peak in late patches was higher in the inducer growth mode and peripheral late patches occurred more frequently in the responder growth mode (Figure 3 E; inducer-responder: $p = 0.10$, Wilcoxon rank sum test). In this metric, the RPE stood out from the NR and both simulated conditions (RPE-inducer: $p = 6.94 \cdot 10^{-5}$; RPE-responder: $p = 0.04$, Wilcoxon rank sum test), indicating a high degree of fragmentation and thus cell division variability.

Together, these data show that NR and RPE have different degrees of variability in cell division timing. The NR displayed lower variability consistent with the simulated inducer growth mode, while the RPE showed higher levels of variability that even exceeded what we modelled with the responder growth mode. Thus, our data support a model where NR and RPE concertedly expand relying on different growth modes, which manifest in differently shaped ArCoS.

Stem- and progenitor cell domains are an emergent property of the system

Both the NR and simulations displayed a cluster of late patches in the central post-embryonic retina (Figure 3 E). Additionally, when discounting late patches, the distribution of patch length showed clear bimodality (Figure 3-figure supplement 2 B), suggesting that beyond fragmentation an additional stochastic process took place after clonal labelling. The region at the border to the embryonic retina, the “induction ring”, marks the original position of the CMZ at the timepoint of Cre-mediated recombination (Figure 4 E). To investigate the stem cell dynamics in the induction ring we turned to the simulation.

Surprisingly, the virtual induction ring contained many few-cell clones unrelated to any ArCoS (Figure 4 A’, encircled by pink dashed lines). In these clones, all stem cells left the niche and thus differentiated (“terminated clones”). Nested inductions showed that sister stem cells within one clone segregated into subclones (Figure 4 A’-A’’, highlighted ArCoS). However, only some of these subclones generated virtual ArCoS. Again, terminated clones clustered in the virtual induction ring (Figure 4 A’’, encircled by black dashed lines), demonstrating that the pattern repeated itself regardless of the timepoint of virtual induction. Therefore, since central positions were occupied by short terminated clones, many stripe-like patches necessarily began in more peripheral positions, explaining the peak in late arising patches.

In our model, all proliferative cells were equipotent stem cells. Nevertheless, a subset of these virtual stem cells proliferated only a few times before terminally differentiating, resulting in a bimodal distribution of patch lengths (Figure 3-figure supplement 2 B). Notably, the overwhelming majority of virtual ArCoS emerged from the periphery of the induction ring (Figure 4 A’-A’’; Video 4), as confirmed by tracing back the position of the founder stem cells at simulation step 0, while centrally located cells formed exclusively terminated clones (Figure 4 B). This behavior is highly reminiscent of retinal progenitor cells *in vivo*, which are believed to reside in the central CMZ (Raymond *et al.*, 2006; Shi *et al.*, 2017). Strikingly, only a minority of virtual stem cells formed ArCoS, while the vast majority formed terminated clones (Figure 4 B).

Together, these data show that the virtual stem cell population subdivided into two functional domains that mirror the current model of the retinal niche with a peripheral stem- and a central progenitor domain (Raymond *et al.*, 2006; Shi *et al.*, 2017). Importantly, this subdivision was not imposed onto the simulation, but emerged dynamically. The central-most cells were poised to differentiate by being pushed out of the niche by divisions of their more peripheral neighbors. This neutral competition occurred continuously, as demonstrated by nested virtual inductions (Figure 4 A’-A’’). Thus, the spatial segregation of stem- and progenitor domains is an emergent property of the system.

Experimental clones follow a spatially biased stochastic drift

Our simulations uncovered a role of stochastic drift in the niche, and lead us to the following two predictions: First, a large proportion of stem cells is lost by neutral competition and forms terminated clones. Thus, ArCoS should be a minority among labelled clones. Second, there is a spatial bias in this drift: The majority of ArCoS will derive from peripheral cells but some will derive from more central positions. Similarly, the majority of terminated clones will derive from central positions, but some will derive from peripheral positions.

To address these predictions experimentally, we again labelled NR stem cells in hatchlings using the Rx2::^{ERT2}Cre, Gaudí^{RSG} line (Centanin *et al.*, 2014; Reinhardt *et al.*, 2015), which when recombined results in a nuclear GFP signal, and analyzed the eyes at adult stage. Few-cell clusters in the induction ring vastly outnumbered ArCoS, showing that terminated clones were the most common type of clone (n=1129 terminated clones in 20 retinae; Figure 4 C'-C'', Figure 4-figure supplement 1 A-B). A small fraction of terminated clones extended into the post-embryonic retina (Figure 4 C'-C'', yellow arrowheads). ArCoS, which by definition always reach the retinal margin, were less frequent (Figure 4 C'-C'', pink arrowheads; n = 36 ArCoS in 20 retinae). Thus, Rx2-expressing cells in the CMZ included cells that proliferated indefinitely as well as cells that proliferated only a few times before differentiating. The preponderance of terminated clones shows that ArCoS-forming cells are a minority, in line with our first prediction.

To address the spatially biased stochastic drift, we examined at which position in the induction ring clones contained their central-most pixels in experiment and simulation (Figure 4 C'-C'', D'-D'', F). Among terminated clones, the majority started in central positions (experiment: 77.3%; simulation: 61.0%), while a minority were exclusively located in the peripheral induction ring or in the post-embryonic retina (experiment: 22.7%; simulation: 39.0%). The difference in proportions between experiment and simulation may indicate that the simulation underestimates the number of terminated clones. Nevertheless, a sizeable subset of experimental terminated clones derived from the periphery of the stem cell domain of the CMZ, indicating that some stem cells drifted into a progenitor-like state.

Among experimental ArCoS, the vast majority (86.1%) started in the periphery, but 13.9% derived from a central position, showing that some cells located in the central progenitor domain of the CMZ drifted into a lifelong stem cell fate. Strikingly, the ratios for peripheral and central ArCoS in the simulation are nearly identical ($p = 1.00$, 2-sample test for equality of proportions), showing that the simulation captures ArCoS dynamics extremely well. Together, these data support a model of stochastic drift with a peripheral-stem and central-progenitor bias that is conditioned by the physical topology of the niche.

<u>NR stem cells undergo radial divisions at the rate predicted by shape regulation</u>

NR ArCoS formed stripes that appeared slightly narrower than in the simulation (Figure 3 A'-A'', C'-C''). In simulations, the division axis was not oriented ("random division axis"). The thin clonal stripes suggested that NR stem cells had a preferential axis of division along the radial (central-peripheral) coordinate, while circumferential divisions occurred with lower frequency than expected for a random division axis orientation.

We wondered whether NR stem cell division orientation could relate to shaping the organ. An inducer growth mode does not necessarily imply regulation of organ shape. To use an analogy, a mass of dough grows from within (similar to the inducer growth mode), but its shape can be imposed externally by a mold (*i.e.* the dough does not affect shape regulation). In the NR, the shape could plausibly be imposed externally by any of the surrounding tissues, and in this case, it would have no role in organ shape regulation (Figure 5 A). As the space available for cells is imposed externally, any orientation of division axes is theoretically possible; after division cells will locally shift to optimally fill space. In an alternative scenario, organ shape could be regulated by oriented cell divisions of CMZ stem cells (Figure 5 B'). In this scenario, a precise orientation of division axes is necessary.

We calculated the ideal proportion of circumferential and radial divisions required to maintain hemispherical geometry. We assumed two principal axes of division, and that each new cell contributed either to the area of the CMZ or to the rest of the eye (Figure 5 B''). Circumferential divisions (two daughter cells stay in the CMZ) must be balanced by radial divisions (one daughter cell is poised to leave the niche and differentiate). A hemispherical eye of radius *R* has the area

$$A_{\text{eye}} = 2\pi R^2 \ , \tag{1}$$

while the CMZ forms a band of width *w* at the base of the eye with area

$$A_{\text{CMZ}} = 2\pi R w \ . \tag{2}$$

Thus, we obtain an ideal ratio of circumferential to radial divisions of

$$1 : \frac{A_{\text{eye}} - A_{\text{CMZ}}}{A_{\text{CMZ}}} \ ,$$

$$1 : \frac{R - w}{w} \ , \tag{3}$$

i.e. for every 1 circumferential division, there must be $\frac{R - w}{w}$ radial divisions. Since $R \gg w$, radial divisions must be more frequent than circumferential divisions, and the frequency of radial divisions increases as the retinal radius grows.

To quantify circumferential stem cell divisions in experimental and simulated data, we took advantage of the exquisite temporal order of NR growth to measure ArCoS width – a proxy for circumferential stem cell divisions. To this end, we developed a pipeline that unrolled the retina as described before, and measured the number of pixels along each radial position normalized by the total circumference – effectively the angle enclosed by two rays traversing the center of the embryonic retina and the clone boundaries at every radial position (Figure 5 D''). To only include lifelong stem cells, we focused our analysis on the post-embryonic retina and excluded the central portion including the induction ring.

As expected, with increasing probability to divide along the circumferential axis, average clone width increases in the simulation (Figure 5-figure supplement 1 A'-B). When division axes perfectly match the ratio in Equation 3, the simulation becomes the limiting case of shape regulation where the hemispherical shape is always maintained. Thus, we modelled how the "ideal division axis" ratio given by Equation 3 affected simulated ArCoS in the inducer growth mode and compared this to experimental data as well as simulations with random division axis (Figure 5 C'-C''').

Experimental ArCoS width averaged to 4.87° (Figure 5 D' black graph; n = 99 ArCoS across 7 retinae). In contrast to experimental data, ArCoS width in simulations with random division axis averaged to 7.28° (Figure 5 D' blue graph; n = 102 clones from 5 simulation runs; compared to experimental data: $p = 1.94 \cdot 10^{-7}$, Welch two-sample t-test). In simulations with ideal division axis, ArCoS width closely matched experimental data, averaging at 4.54° (Figure 5 D', red graph; n = 133 clones from 5 simulation runs; compared to experimental data: p = 0.37, Welch two-sample t-test).

These data show that NR stem cell divisions were not randomly oriented, but instead were preferentially oriented along the central-peripheral axis. Moreover NR stem cells underwent radial and circumferential divisions at a rate consistent with a role in organ shape regulation.

Local biases in ventral NR stem cell divisions influence retinal topology

We observed that in the retina of the surface-dwelling medaka, the position of the embryonic retina was not centered, but instead was shifted ventrally (Figure 6 A'). As a result, the post-embryonic retina was longer dorsally than ventrally (ratio dorsal to ventral length: mean = 1.42; standard deviation = 0.29; n = 10 retinae). The embryonic retina covered the entire retinal surface at induction (Figure 6 A''). Equal growth around the circumference should maintain the embryonic retina in the center. The ventral-ward shift indicated that along the CMZ circumference, ventral stem cells had different division parameters.

We probed the feasibility of different scenarios in generating a ventral shift in an *in silico* screen. First, we discerned two ways for stem cells in the ventral domain (defined as a 90°

sector; Figure 6-figure supplement 2) to select a different division behavior: Either a lineage-bound intrinsic signal (*e.g.* epigenetic imprinting), or a lineage-independent extrinsic signal (*e.g.* a local diffusible molecule). Second, we altered two cell division parameters: The probability of division, which we varied between half ($p_{\text{div\_ventral}} = 0.5 \cdot p_{\text{div\_non-ventral}}$) or equal to the value in the non-ventral sector ($p_{\text{div\_ventral}} = p_{\text{div\_non-ventral}}$), and the preferential axis of cell division, which we varied between circumferentially-biased ($p_{\text{circ\_ventral}} = 1$) and radially-biased ($p_{\text{circ\_ventral}} = 0$).

In control simulations where all cells behaved equally, the embryonic retina stayed centered (Figure 6 B', C'). For a lineage-bound intrinsic signal, a circumferential bias lead to massive enlargement of ventral lineages at the expense of adjacent clones without affecting the embryonic retina (Figure 6 B''). Reducing proliferation probability resulted in termination of ventral lineages, as adjacent clones displaced them from the virtual niche (Figure 6 B'''). An intrinsic signal resulted in a ventral shift only if circumferential bias was combined with lower proliferation probability (Figure 6 B'''' – condition I). In these simulations, circumferential divisions allowed ventral lineages to physically occupy niche positions (preventing their displacement) while lower proliferation reduced pressure on cells of the embryonic retina, allowing a ventral shift. In the scenario of a lineage-independent extrinsic signal, two conditions resulted in a ventral shift of the embryonic retina: Both lower division probability (Figure 6 C''' – condition II) and the combination of lower division probability with circumferential division axis bias (Figure 6 C'''' – condition III).

To identify which scenario was most plausible, we analyzed patches in the ventral and non-ventral sectors. Both in experiments and all three simulated conditions, patch shape in the non-ventral sector was similar (Figure 6 D'-D''''). Although there was a tendency for ventral clones to terminate more often, the width distribution of experimental NR patches did not differ substantially between non-ventral and ventral sectors (Figure 6 D', E', Figure 6-figure supplement 1 D'; p = 0.84, Wilcoxon rank sum test). In contrast, this latter criterion was violated by two of the three simulated scenarios (Figure 6 D''-D'''' and E''-E'''', Figure 6-figure supplement 1 D''-D'''').

In condition I, ventral ArCoS started narrow but then broadened (Figure 6 E'') and interdigitated circumferentially (Figure 6-figure supplement 1 A, black arrowheads), unlike the very uniform stripes in the experimental data. The broader ventral ArCoS lead to a more dispersed distribution compared to the non-ventral sector (Figure 6-figure supplement 1D''; p = $4.31 \cdot 10^{-14}$, Wilcoxon rank sum test). In condition II, the majority of ventral ArCoS formed very narrow stripes, but at the border to the non-ventral sector ArCoS were broad and curved (Figure 6-figure supplement 1 B, black arrowheads). Again, this resulted in more shape

variation (Figure 6 E’’’). Nevertheless, these outliers were outweighed by a high density of narrow clones, such that the overall distribution was similar between ventral and non-ventral sectors (Figure 6-figure supplement 1 D’’’; $p = 0.12$, Wilcoxon rank sum test). Clones in the ventral and non-ventral sectors were qualitatively similar in condition III (Figure 6 E’’’’, Figure 6-figure supplement 1 C). Ventral clones however tended to be broader, resulting in a more dispersed distribution compared to the non-ventral sector (Figure 6-figure supplement 1 D’’’’; $p = 8.90 \cdot 10^{-10}$, Wilcoxon rank sum test).

In conclusion, ventral NR stem cells have a different behavior than elsewhere along the circumference, leading to a ventral-ward shift of the embryonic retina. The simulations suggest that this different behavior consists of modulation of proliferation parameters by an extrinsic signal in the ventral CMZ.

Discussion

The NR drives growth upstream of the RPE

The coordinated growth of multiple independent tissues is a ubiquitous process in biology. In this work, we used the post-embryonic growth of NR and RPE in the eye of medaka as a model system of coordination in an organ where both growth and shape must be precisely regulated.

Eye size in fish scales to the body size (Lyall, 1957; Johns and Easter, 1977). Body size, and thus eye growth rates greatly vary among individuals and depend on environmental factors (Johns, 1981). This natural malleability implies that feedback coupling plays a dominant role rather than the precise parametrization of each tissue growth and cell proliferation rate. Our simulations showed that inducer and responder growth modes impacted on variability in cell division timing, ultimately resulting in distinct clonal patterns that reproduced the experimentally observed differences between NR and RPE.

RPE cells divided with high variability, indicative of periods of long quiescence where they waited for proliferative cues. NR cells displayed lower variability, supporting an upstream role in regulating growth (Figure 7 A). Although our implementation of the responder growth mode used a mechanical stimulus (local cell density), a biochemical stimulus could equally well represent the system.

Our model highlights an underappreciated mechanism whereby tissues coordinate by inducer and responder roles. Such division of labor among tissues might apply more generally to multiple organ systems, *e.g.* hair follicle cells in mouse induce the growth of underlying adipose tissue through hedgehog signalling (Zhang *et al.*, 2016). Intriguingly, hedgehog signalling also regulates the NR/RPE boundary in the CMZ of medaka (Reinhardt *et al.*, 2015), suggesting that signals mediating coordination of proliferative cell populations might be conserved.

Multipotent progenitor cells are stem cells that were outcompeted

The topology of the retinal niche lead to a spatially biased neutral drift where stem and progenitor compartments spontaneously emerged. All virtual cells had equal potency, yet only a fraction realized their full stem cell potential. Peripheral cells had a high chance to become canalized in a stem cell fate, while central cells were more likely to act as progenitor cells with limited proliferation potential (Figure 7 B).

Our experimental data support a spatially biased neutral drift. Fusion of clones may have lead us to overestimate ArCoS deriving from the central domain, which represent progenitors reverting to a stem cell fate. Nevertheless, terminated clones arising from the very periphery

of the niche unambiguously demonstrate that some stem cells failed to self-renew throughout the life of the animal. Moreover, our finding that only cells in the first two rows of the CMZ have stem cell potential is consistent with *in vivo* time-lapse data (Wan *et al.*, 2016; Tang *et al.*, 2017). Interestingly, retrograde movement of row 2 cells into row 1 of the CMZ occurs *in vivo* (Wan *et al.*, 2016), which we also observed in our simulations.

CMZ progenitor cells can be subdivided into two populations (Harris and Perron, 1998; Raymond *et al.*, 2006): First, peripheral multipotent progenitors (*i.e.* able to generate all retinal neurons and glia) which differ from stem cells only in their proliferative potential. Second, central progenitors that are restricted both in proliferative and differentiation potential, which likely act as a transit-amplifying zone, both increasing the proliferative output and cross-regulating to produce a full neuronal complement with the correct proportions of cell types (Perez-Saturnino *et al.*, 2018).

Our data support an alternative model that identifies peripheral multipotent progenitors as stem cells that have been outcompeted. All terminated clones we examined were multipotent and spanned all retinal layers (Figure 1 Supplement 2). Thus, as in many other systems (Clevers and Watt, 2018), our work highlights the limitation of strictly defining stem cells as infinitely self-renewing, or *a posteriori* based on their ArCoS-forming capacity.

Importantly, although stochastic competition is most apparent in the early phase after clonal induction, it occurs continuously as demonstrated by late arising patches (Figure 3 E) and nested inductions (Figure 4 A'-A''). The shift from an "early stochastic" to "late polyclonal" growth observed in other systems (Nguyen *et al.*, 2017) may simply result from clonal growth masking the underlying stochasticity. Due to this stochasticity, it is impossible to tell at any moment with absolute certainty if a given cell will perpetually function as a stem cell.

Why does the CMZ niche of the retina not drift to monoclonality?

Neutral drift in a finite-sized environment such as adult mammalian tissues must ultimately result in a monoclonal niche (Snippert *et al.*, 2010; Colom and Jones, 2016; Clevers and Watt, 2018). In fish, homeostatic growth expands niches, and thus the number of stem cells increases (Centanin *et al.*, 2011). In principle, niche expansion reduces the impact of competition on clonal loss, but does not completely abolish it.

Indeed, neutral drift leads to gradual loss of polyclonality in the intestine and muscle of fish (Aghaallaei *et al.*, 2016; Nguyen *et al.*, 2017). Organs may limit monoclonal drift by physically isolating niches (Aghaallaei *et al.*, 2016). In the intestine of both mammals and fish, physical isolation of multiple niches results in a polyclonal organ built up of monoclonal units (Snippert *et al.*, 2010; Aghaallaei *et al.*, 2016). In contrast, the CMZ is a physically contiguous niche that nevertheless maintains polyclonality lifelong both in the NR and the RPE (Centanin *et*

al., 2011, 2014). As shown in this work, the retina is not devoid of stochastic competition. Then how does it conserve its polyclonality?

Conceptually, the clonal growth of the retina resembles a population expanding into a new habitat, as studied in the context of evolutionary theory (Hallatschek and Nelson, 2010). Specifically for a radially expanding population, it has been mathematically proven that (assuming pure neutral genetic drift) no single clone will ever take over and clonal sectors perpetually coexist (Hallatschek and Nelson, 2010; Korolev *et al.*, 2012). Growth of the perimeter is faster than circumferential expansion of clones, thus preserving population diversity (Hallatschek and Nelson, 2010). Interestingly, in the NR, the biased division axis further reduces competition (Figure 5), thus increasing niche polyclonality. In summary, the geometry of the CMZ niche prohibits the total loss of polyclonality.

The NR senses the retinal radius and directs cell divisions to adapt organ shape

Our analysis of NR cell divisions implies that cells sense the radius of the eye to regulate organ shape. Across vertebrates, the retina integrates visual input to adapt organ shape to optimize optics, a process called “emmetropization” (Wallman and Winawer, 2004). In chicken, emmetropization is regulated by specialized neurons distributed across the retina that send their axons to the CMZ, implicating the CMZ in regulation of eye shape (Fischer *et al.*, 2008). Visual cues also guide emmetropization in fish (Kröger and Wagner, 1996; Shen *et al.*, 2005; Shen and Sivak, 2007). Eye growth in young fish predominantly occurs by cell addition, while in older fish CMZ proliferation decreases (Johns, 1981) coincident with a decrease in emmetropization plasticity (Shen and Sivak, 2007). Thus, in fish, emmetropization correlates with CMZ proliferation.

Experiments in chicken and zebrafish support the existence of two principal axes of stem cell division, *i.e.* circumferential and central-peripheral (Fischer *et al.*, 2008; Ritchey *et al.*, 2012; Wan *et al.*, 2016). Notably, the predominance of central-peripheral divisions and decreasing frequency over time of circumferential divisions in CMZ stem cells that is predicted by Equation 3 is supported by *in vivo* imaging data (Wan *et al.*, 2016) and previous long-term clonal analyses (Centanin *et al.*, 2014). Altogether, the data support a model where the NR perceives the retinal radius through visual cues, and that cell divisions in the NR contribute to shaping the eye.

An eye-internal signal directs local proliferation parameters in the CMZ

The retinae of many fishes grow asymmetrically, perhaps to maintain the relative positions of receptive fields of neurons (Johns, 1977, 1981; Easter, 1992). Ecology dictates a distribution of subdomains enriched in specialized neuronal circuits and retinal cell subtypes (Zimmermann *et al.*, 2018). Interestingly, in green sunfish, the area that grows slowest

displays highest visual acuity (Cameron, 1995). Medaka predominantly gaze upwards in their native shallow rice paddies, and a higher ventral acuity has been presumed based on photoreceptor densities (Nishiwaki *et al.*, 1997). Thus, slower ventral growth may have evolved to match ecological requirements for medaka vision.

Our *in silico* screen identified three scenarios consistent with asymmetric ventral growth. Based on clonal patterns, an extrinsic signal driving lower proliferation (and potentially also circumferential divisions) appears most plausible. Experimental eye re-orientation *in vivo* implied an eye-internal mechanism independent on body axes or visual cues in regulating asymmetric retinal growth (Cameron, 1996). The origin of this signal and how it scales with the growing eye to always affect a similarly-sized retinal sector remains to be elucidated.

The CMZ integrates cues to direct eye growth and shape

The retina integrates global systemic cues such as nutrition to scale with body size (Johns and Easter, 1977), local eye-internal cues to generate an asymmetric retinal topology (Cameron, 1996), and external visual cues to adapt the shape of the organ (Kröger and Wagner, 1996; Shen and Sivak, 2007). In chicken and goldfish, visual cues and nutrients feed into the CMZ through growth factor signalling (Boucher and Hitchcock, 1998; Fischer *et al.*, 2008; Ritchey *et al.*, 2012). We propose that NR cells in the CMZ act as a hub to coordinate organ growth; in the eye of fish, this happens at the level of cell proliferation parameters, which affect eye growth, eye shape, and retinal topology (Figure 7 C).

Indeterminate, lifelong growth is a widespread evolutionary strategy (Karkach, 2006). Given the geometrical constraints of the eye with respect to optics, a peripheral proliferative domain is the most parsimonious architecture to ensure that the differentiated neuronal cell mosaic is not disturbed by constant proliferation. Fishes are the largest vertebrate clade, with a huge diversity of eye shapes, such as cylindrical eyes in deep-sea fish (Fernald, 1990). By modulating CMZ proliferation parameters, evolution can adapt whole-organ morphogenesis to perfectly fit to the species' ecological niche.

References:

Aghaallaei, N., Gruhl, F., Schaefer, C.Q., Wernet, T., Weinhardt, V., Centanin, L., et al. (2016) Identification, visualization and clonal analysis of intestinal stem cells in fish. *Development* **143**: 3470–3480.

Amato, M.A., Arnault, E., and Perron, M. (2004) Retinal stem cells in vertebrates: Parallels and divergences. *Int. J. Dev. Biol.* **48**: 993–1001.

Beck, J.C., Gilland, E., Tank, D.W., and Baker, R. (2004) Quantifying the ontogeny of optokinetic and vestibuloocular behaviors in zebrafish, medaka, and goldfish. *J. Neurophysiol.* **92**: 3546–61.

Boucher, S.E. and Hitchcock, P.F. (1998) Insulin-related growth factors stimulate proliferation of retinal progenitors in the goldfish. *J. Comp. Neurol.* **394**: 386–94.

Buchmann, A., Alber, M., and Zartman, J.J. (2014) Sizing it up: The mechanical feedback hypothesis of organ growth regulation. *Semin. Cell Dev. Biol.* **35**: 73–81.

Buske, P., Galle, J., Barker, N., Aust, G., Clevers, H., and Loeffler, M. (2011) A comprehensive model of the spatio-temporal stem cell and tissue organisation in the intestinal crypt. *PLoS Comput. Biol.* **7**: e1001045.

Cameron, D.A. (1996) Asymmetric retinal growth: Evidence for regulation by a retinotopic mechanism. *Vis. Neurosci.* **13**: 493.

Cameron, D.A. (1995) Asymmetric retinal growth in the adult teleost green sunfish (Lepomis cyanellus). *Vis. Neurosci.* **12**: 95–102.

Centanin, L., Ander, J.-J., Hoeckendorf, B., Lust, K., Kellner, T., Kraemer, I., et al. (2014) Exclusive multipotency and preferential asymmetric divisions in post-embryonic neural stem cells of the fish retina. *Development* **141**: 3472–3482.

Centanin, L., Hoeckendorf, B., and Wittbrodt, J. (2011) Fate restriction and multipotency in retinal stem cells. *Cell Stem Cell* **9**: 553–562.

Clevers, H. and Watt, F.M. (2018) Defining Adult Stem Cells by Function, Not by Phenotype. *Annu. Rev. Biochem.* **87**: annurev-biochem-062917-012341.

Colom, B. and Jones, P.H. (2016) Clonal analysis of stem cells in differentiation and disease. *Curr. Opin. Cell Biol.* **43**: 14–21.

Droujinine, I.A. and Perrimon, N. (2016) Interorgan Communication Pathways in Physiology: Focus on Drosophila. *Annu. Rev. Genet.* **50**: 539–270.

Easter, S.S. (1992) Retinal growth in foveated teleosts: nasotemporal asymmetry keeps the fovea in temporal retina. *J. Neurosci.* **12**: 2381–92.

Fernald, R.D. (1990) The optical system of fishes. In, Douglas,R. and Djamgoz,M. (eds), *The Visual System of Fish*. Springer Netherlands, pp. 45–61.

Fischer, A.J., Ritchey, E.R., Scott, M.A., and Wynne, A. (2008) Bullwhip neurons in the retina regulate the size and shape of the eye. *Dev. Biol.* **317**: 196–212.

Fukamachi, S., Asakawa, S., Wakamatsu, Y., Shimizu, N., Mitani, H., and Shima, A. (2004) Conserved function of medaka pink-eyed dilution in melanin synthesis and its divergent transcriptional regulation in gonads among vertebrates. *Genetics* **168**: 1519–1527.

Hallatschek, O. and Nelson, D.R. (2010) Life at the front of an expanding population. *Evolution (N. Y).* **64**: 193–206.

Harris, W.A. and Perron, M. (1998) Molecular recapitulation: the growth of the vertebrate retina. *Int. J. Dev. Biol.* **42**: 299–304.

Johns, P.R. (1981) Growth of fish retinas. *Am. Zool.* **21**: 447–458.

Johns, P.R. (1977) Growth of the adult goldfish eye. III. Source of the new retinal cells. *J. Comp. Neurol.* **176**: 343–57.

Johns, P.R. and Easter, S.S. (1977) Growth of the adult goldfish eye. II. Increase in retinal cell number. *J. Comp. Neurol.* **176**: 331–41.

Karkach, A.S. (2006) Trajectories and models of individual growth. *Demogr. Res.* **15**:.

Klein, A.M., Doupé, D.P., Jones, P.H., and Simons, B.D. (2007) Kinetics of cell division in epidermal maintenance. *Phys. Rev. E* **76**:.

Korolev, K.S., Müller, M.J.I., Karahan, N., Murray, A.W., Hallatschek, O., and Nelson, D.R. (2012) Selective sweeps in growing microbial colonies. *Phys. Biol.* **9**:.

Kröger, R.H.H. and Wagner, H.-J. (1996) The eye of the blue acara (Aequidens pulcher, Cichlidae) grows to compensate for defocus due to chromatic aberration. *J. Comp. Physiol. A* **179**: 837–842.

Li, X., Upadhyay, A.K., Bullock, A.J., Dicolandrea, T., Xu, J., Binder, R.L., et al. (2013) Skin Stem Cell Hypotheses and Long Term Clone Survival - Explored Using Agent-based Modelling. *Sci. Rep.* **3**: 1904.

Lischik, C.Q., Adelmann, L., and Wittbrodt, J. (2018) Enhanced in vivo-imaging in fish by optimized anaesthesia, fluorescent protein selection and removal of pigmentation. *bioRxiv*. https://doi.org/10.1101/428763

Loosli, F., Köster, R.W., Carl, M., Kühnlein, R., Henrich, T., Mücke, M., et al. (2000) A genetic screen for mutations affecting embryonic development in medaka fish (Oryzias latipes). *Mech. Dev.* **97**: 133–9.

Lui, J.C. and Baron, J. (2011) Mechanisms Limiting Body Growth in Mammals. *Endocr. Rev.* **32**: 422–440.

Lust, K. and Wittbrodt, J. (2018) Activating the regenerative potential of Müller glia cells in a regeneration-deficient retina. *Elife* **7**: 1–23.

Lyall, A.H. (1957) The growth of the trout retina. *Q. J. Microsc. Sci.* **98**: 101–110.

Nguyen, P.D., Gurevich, D.B., Sonntag, C., Hersey, L., Alaei, S., Nim, H.T., et al. (2017) Muscle Stem Cells Undergo Extensive Clonal Drift during Tissue Growth via Meox1-Mediated Induction of G2 Cell-Cycle Arrest. *Cell Stem Cell* **21**: 107–119.e6.

Nishiwaki, Y., Oishi, T., Tokunaga, F., and Morita, T. (1997) Three-Dimensional Reconstitution of Cone

662 Arrangement on the Spherical Surface of the Retina in the Medaka Eyes. *Zoolog. Sci.* **14**: 795–801.
663 Ohki, H. and Aoki, K. (1985) Development of Visual Acuity in the Larval medaka, Oryzias latipes. *Zoolog. Sci.* **2**:
664 123–126.
665 Osborne, J.M., Fletcher, A.G., Pitt-Francis, J.M., Maini, P.K., and Gavaghan, D.J. (2017) Comparing individual-
666 based approaches to modelling the self-organization of multicellular tissues. *PLoS Comput. Biol.* **13**:
667 e1005387.
668 Osborne, J.M., Walter, A., Kershaw, S.K., Mirams, G.R., Fletcher, A.G., Pathmanathan, P., et al. (2010) A hybrid
669 approach to multi-scale modelling of cancer. *Philos. Trans. R. Soc. A Math. Phys. Eng. Sci.* **368**: 5013–
670 5028.
671 Pathmanathan, P., Cooper, J., Fletcher, A., Mirams, G., Murray, P., Osborne, J., et al. (2009) A computational
672 study of discrete mechanical tissue models. *Phys. Biol.* **6**:.
673 Perez-Saturnino, A., Lust, K., and Wittbrodt, J. (2018) Notch signalling patterns retinal composition by regulating
674 atoh7 during post-embryonic growth. *Development* **145**: dev169698.
675 Phansalkar, N., More, S., Sabale, A., and Joshi, M. (2011) Adaptive local thresholding for detection of nuclei in
676 diversity stained cytology images. *ICCSP 2011 - 2011 Int. Conf. Commun. Signal Process.* 218–220.
677 R Core Team (2015) R: A Language and Environment for Statistical Computing.
678 Raymond, P.A., Barthel, L.K., Bernardos, R.L., and Perkowski, J.J. (2006) Molecular characterization of retinal
679 stem cells and their niches in adult zebrafish. *BMC Dev. Biol.* **6**: 1–17.
680 Reinhardt, R., Centanin, L., Tavhelidse, T., Inoue, D., Wittbrodt, B., Concordet, J.-P., et al. (2015) Sox2, Tlx, Gli3,
681 and Her9 converge on Rx2 to define retinal stem cells in vivo. *EMBO J.* **34**: 1572–1588.
682 Ritchey, E.R., Zelinka, C.P., Tang, J., Liu, J., and Fischer, A.J. (2012) The combination of IGF1 and FGF2 and
683 the induction of excessive ocular growth and extreme myopia. *Exp. Eye Res.* **99**: 1–16.
684 Roselló-Díez, A. and Joyner, A.L. (2015) Regulation of long bone growth in vertebrates; it is time to catch up.
685 *Endocr. Rev.* **36**: 646–680.
686 Schindelin, J., Arganda-Carreras, I., Frise, E., Kaynig, V., Longair, M., Pietzsch, T., et al. (2012) Fiji: An open-
687 source platform for biological-image analysis. *Nat. Methods* **9**: 676–682.
688 Shen, W. and Sivak, J.G. (2007) Eyes of a lower vertebrate are susceptible to the visual environment. *Investig.*
689 *Ophthalmol. Vis. Sci.* **48**: 4829–4837.
690 Shen, W., Vijayan, M., and Sivak, J.G. (2005) Inducing form-deprivation myopia in fish. *Investig. Ophthalmol. Vis.*
691 *Sci.* **46**: 1797–1803.
692 Shi, D., Tavhelidse, T., Thumberger, T., Wittbrodt, J., and Greb, T. (2017) Bifacial stem cell niches in fish and
693 plants. *Curr. Opin. Genet. Dev.* **45**: 28–33.
694 Snippert, H.J., van der Flier, L.G., Sato, T., van Es, J.H., van den Born, M., Kroon-Veenboer, C., et al. (2010)
695 Intestinal crypt homeostasis results from neutral competition between symmetrically dividing Lgr5 stem
696 cells. *Cell* **143**: 134–144.
697 Stemmer, M., Thumberger, T., Del Sol Keyer, M., Wittbrodt, J., and Mateo, J.L. (2015) CCTop: An intuitive,
698 flexible and reliable CRISPR/Cas9 target prediction tool. *PLoS One* **10**: 1–11.
699 Stenkamp, D.L. (2007) Neurogenesis in the Fish Retina. *Int. Rev. Cytol.* **259**: 173–224.
700 Sütterlin, T., Kolb, C., Dickhaus, H., Jäger, D., and Grabe, N. (2013) Bridging the scales: Semantic integration of
701 quantitative SBML in graphical multi-cellular models and simulations with EPISIM and COPASI.
702 *Bioinformatics* **29**: 223–229.
703 Sütterlin, T., Tsingos, E., Bensaci, J., Stamatas, G.N., and Grabe, N. (2017) A 3D self-organizing multicellular
704 epidermis model of barrier formation and hydration with realistic cell morphology based on EPISIM. *Sci.*
705 *Rep.* **7**: 1–11.
706 Sütterlin, T, 2019, EPISIM-Simulator, GitLab, https://gitlab.com/EPISIM/EPISIM-Simulator, 70940534
707 Tang, X., Gao, J., Jia, X., Zhao, W., Zhang, Y., Pan, W., and He, J. (2017) Bipotent progenitors as embryonic
708 origin of retinal stem cells. *J. Cell Biol.* **216**: 1833–1847.
709 Wallman, J. and Winawer, J. (2004) Homeostasis of eye growth and the question of myopia. *Neuron* **43**: 447–
710 468.
711 Wan, Y., Almeida, A.D., Rulands, S., Chalour, N., Muresan, L., Wu, Y., et al. (2016) The ciliary marginal zone of
712 the zebrafish retina: clonal and time-lapse analysis of a continuously growing tissue. *Development* **143**:
713 1099–1107.
714 Watt, F.M. and Hogan, B.L. (2000) Out of Eden: stem cells and their niches. *Science* **287**: 1427–30.
715 Zhang, B., Tsai, P.C., Gonzalez-Celeiro, M., Chung, O., Boumard, B., Perdigoto, C.N., et al. (2016) Hair follicles'
716 transit-amplifying cells govern concurrent dermal adipocyte production through sonic hedgehog. *Genes*
717 *Dev.* **30**: 2325–2338.
718 Zimmermann, M.J.Y., Nevala, N.E., Yoshimatsu, T., Osorio, D., Nilsson, D.E., Berens, P., and Baden, T. (2018)
719 Zebrafish Differentially Process Color across Visual Space to Match Natural Scenes. *Curr. Biol.* **28**: 2018–
720 2032.e5.
721

Materials and Methods:

1. Key resources table

Reagent type (species) or resource	Designation	Source or reference	Identifiers	Additional information
Strain (*Oryzias latipes*)	Cab	(Loosli *et al.*, 2000)		wildtype inbred strain derived fom wild medaka Southern population
Strain (*O. latipes*)	Rx2::$^{ER T2}$Cre, Gaudí^{RSG}	(Centanin *et al.*, 2014; Reinhardt *et al.*, 2015)		
Strain (*O. latipes*)	Rx2::$^{ER T2}$Cre, Gaudí$^{2.1}$	(Centanin *et al.*, 2014; Reinhardt *et al.*, 2015)		
Strain (*O. latipes*)	LoxP^{-OUT}	(Centanin *et al.*, 2014)		Derived from recombined gametes of Ubi::Gaudí^{RSG}.
Sequence-based reagent	short guide RNAs against Oca2	this paper		target sites: GAAACCCAGGTGGCCATTGC[AGG] and TTGCAGGAATCATTCTGTGT[GGG]
Chemical compound, drug	Tamoxifen	Sigma Aldrich	T5648	
Chemical compound, drug	5-Iodo-2′-deoxyuridine (IdU)	Sigma Aldrich	I7756	
Chemical compound, drug	Ethyl 3-aminobenzoate methanesulfonate salt (Tricaine)	Sigma Aldrich	A5040	
Antibody	anti-GFP (chicken, polyclonal)	Life Technologies	A10262	1:200
Antibody	anti-IdU (mouse, monoclonal)	Becton Dickinson	347580	1:25
Antibody	anti-chicken Alexa Fluor 488 (donkey, polyclonal)	Jackson/Dianova	703-545-155	1:200
Antibody	anti-mouse Alexa 546 (goat, polyclonal)	Invitrogen	A-11030	1:400

2. Experimental methods

Animal welfare statement

Medaka (*Oryzias latipes*) fish were bred and maintained as previously established (Loosli *et al.*, 2000). All experimental procedures were performed according to the guidelines of the German animal welfare law and approved by the local government (Tierschutzgesetz §11, Abs. 1, Nr. 1, husbandry permit number AZ 35-9185.64/BH; line generation permit number AZ 35-9185.81/G-145-15).

Clonal lineage labelling

ArCoS in the NR were generated as described previously (Centanin *et al.*, 2011, 2014; Reinhardt *et al.*, 2015). Transplantations were from labelled donor cells of the $LoxP^{OUT}$ line to unlabelled wildtype Cab host blastulae. Cre-mediated recombination was performed in hatchlings by induction of the Rx2::^{ERT2}Cre, Gaudí lines with 5 µM tamoxifen diluted in fish water for at least 3 hours.

For ArCoS in the RPE, mosaic unpigmented clones were generated using CRISPR/Cas9 by injecting 30 ng/µl each of two short guide RNAs directed against the gene Oca2 in one-cell stage Cab medaka embryos. Oca2 is required to produce melanin pigment (Fukamachi *et al.*, 2004; Lischik *et al.*, 2018). The sgRNA was designed using CCTop (Stemmer *et al.*, 2015).

Treatment with IdU

Fish were bathed in fish water containing concentrations of 2.5 mM IdU as previously described (Centanin *et al.*, 2011).

Sample preparation and imaging

Fish were allowed to grow and sacrificed as young adults with an overdose of Tricaine. Whole fish were fixed in 4% formaldehyde in phosphate buffered saline and 0.1% Tween (PTW) at least once overnight at 4°C while gently shaking. Eyes were dissected, if necessary immunostained, and imaged at a Nikon AZ100 upright stereomicroscope using a 5x dry objective.

Immunostaining

To remove melanin pigment, fixed samples were bleached with 0.3% H_2O_2 and 0.5% KOH dissolved in PTW. Samples were permeabilized in acetone for 10 minutes at -20°C. Blocking was performed for at least one hour in a solution of 4% sheep serum, 1% bovine serum albumin (BSA), and 0.1% DMSO, diluted in PTW. Samples were incubated with primary antibodies diluted in 4% sheep serum and 1% BSA in PTW at least once overnight at 4°C with gentle mixing. Secondary antibodies were diluted in 4% sheep serum and 1% BSA in PTW; samples were incubated in secondary antibody solution at least once overnight at 4°C with gentle mixing.

An antigen retrieval step was performed prior to IdU staining. This step consisted of post-fixation in 4% formaldehyde for 1 hour, DNA denaturation with 2M HCl and 0.5% Triton for 45 minutes, and pH recovery for 10 minutes in a 40% borax solution in PTW.

3. Data Analysis

Experimental clone segmentation

All image processing and analysis was performed using the Fiji distribution of ImageJ (Schindelin *et al.*, 2012). Experimental retinae were selected such that only sparsely labelled eyes of comparable size were used for analysis. For NR samples, a maximum intensity projection of confocal stacks was used for segmentation. For RPE samples, a custom script was written to create a focused reconstruction from multiple focal planes based on the hemispherical shape of the whole-mount retina. Briefly, the regions in focus in a stack through a hemispherical object are rings of increasing radii (and a circle in the first plane). The size of these rings was calculated based on the size of the sample. The focused areas were extracted and collated in one composite image.

Labelled clones were segmented by subtracting background noise with a difference of gaussians, and thresholded by the Phansalkar local threshold algorithm as it is implemented in Fiji (Phansalkar *et al.*, 2011). The segmentation was manually curated to eliminate errors.

In silico clonal lineage labelling

For simulating NR clones, all proliferating cells in the model received a unique identifier when the eye radius reached 150 µm. The radius was chosen based on the estimated radius of the NR when genetic recombination was induced *in vivo*. To replicate RPE clones, the virtual labelling experiment began at 100 µm, since mosaic knockout happens at an earlier timepoint in development. The identifier was inherited to daughter cells, allowing to reconstruct a lineage at any time during the simulation.

For comparison to experimental data, between 8-13% of clones were randomly sampled from the full simulated population; the sample was chosen to produce a sparse label with a comparable number of patches per retina as in the experimental data. Each simulation was sampled twice. The sample of simulated clones was plotted as a 2D projection using a custom Python script; cellular edges were blurred by application of a median filter and shape smoothing plugin in ImageJ.

Clone shape complexity

Shape complexity of simulated clones from simulation screenshots was quantified by thresholding individual clones by color, calculating the pixel perimeter, and dividing this value by the pixel perimeter of the smallest bounding rectangle enclosing the clone.

Patch shape analysis

Data analysis on experimental and simulated data was performed using the same automated pipeline in ImageJ, which takes as an input segmented images where the embryonic retina and retinal margin were marked manually. The size of the embryonic retina was estimated based on the induction ring and position of the optic nerve exit, the radius of this estimate was then increased to ensure complete exclusion of all embryonic area. Different sizes of this estimate produced comparable results.

The analysis pipeline first performed a coordinate transform to unroll the retina: Proximal views of experimental and simulated retinae were centered on the embryonic retina, converted to polar coordinates, and finally projected onto a cartesian coordinate system (Figure 3-figure supplement 2 C). After this transform, the width of the image corresponded to the circumference, while the height corresponded to the radius. Radii were normalized to extend from 0% (the border of the embryonic retina; central) to 100% (the retinal margin; peripheral). Patch outlines were automatically extracted and superimposed to generate patch density plots. The “plot profile” function in ImageJ was used to extract average pixel intensities along a rectangle spanning the entire image. Gaussian fit was produced in R (R Core Team, 2015).

Skeletonization of patches for node counting was performed using a custom algorithm tailored to the radially oriented retinal lineages: Segmented patches were broken up into radial segments along normalized radial bins ranging from the embryonic to the retinal margin. Each segment was assigned a skeleton element, and these elements were linked in a final step prior to node counting.

For each patch, the starting position along normalized radial bins was noted. Patches that did not begin in the first radial bin were considered “late arising patches”. Maximum patch width and maximum patch length were obtained by extracting individual patch outlines and computing the width and height of the minimum bounding rectangle, respectively. To exclude small spot-like patches, only patches spanning at least 20% of the radial coordinate were used for the maximum patch width analysis. Late arising patches were excluded from the maximum patch length analysis. These data were used to generate rug plots in R. Statistical analysis was performed in R.

Quantification of the proportion of ArCoS and terminated clones

In simulated data, ArCoS were defined as clones that still retained cells in the virtual CMZ at the final simulation step used for analysis, *i.e.* when the virtual retina had attained a radius of R = 800 µm. All other clones counted as terminated clones. The initial position at simulation step 0 of the founder stem cells for each clone was extracted from the simulated data and assigned to a 5 µm-wide bin corresponding to each of the cell rows in the virtual CMZ.

For the comparison of experimental to simulated data, segmentation was performed as described in “Experimental clone segmentation” and “*In silico* clonal lineage labelling”. The position of the induction ring was estimated based on the following criteria: The inner circle was placed such that it enclosed as many 1-cell clones as possible (*i.e.* labelled differentiated cells in the experimental data). The outer circle was placed such that it enclosed all few-cell clusters and crossed all ArCoS. Variation of the position of these two boundaries produced similar results. The induction circle was split in the middle and each clone was assigned to the central-most or peripheral-most ring based on the position of its central-most pixel.

Width of clones

Both experimental and simulated data were projected onto a rectangular coordinate system as described in “Patch shape analysis”. The width of clones was measured using a custom ImageJ plugin that measures the exact clone width in pixels at every radial coordinate, and normalizes this value to

the circumference of the retina at the corresponding position. These measurements correspond to the angle enclosed by two rays traversing the center of the embryonic retina and the clone boundaries at every radial position (Figure 5 D''). These width measurements were exported for analysis and plotting in R. To evaluate only lifelong stem cell clones, the induction ring and small clones that did not extend more than 10% of the radius past the induction ring were excluded from the analysis. Near the retinal margin, the fluorescent signal tapers off due to the retinal curvature and optical limitations of the imaging setup. Thus, the last 5% of the retinal radius were excluded from the analysis. The mean and 95% confidence interval were calculated for each radial position.

Acknowledgments:

We thank the Wittbrodt department, S. Lemke, U. Schwarz, I. Lebovka, E. Kuchen, R. Hodge, and M. González-Gaitán for critical reading of the manuscript. We thank T. Thumberger and M. Stemmer for their help in designing short guide RNAs for CRISPR/Cas9 experiments. We are grateful to A. Saraceno, E. Leist and M. Majewski for fish husbandry.

Simulations in this work were performed on the computational resource bwUniCluster funded by the Ministry of Science, Research and Arts and the Universities of the State of Baden-Württemberg, Germany, within the framework program bwHPC.

The authors declare no competing financial interests. Correspondence and requests for materials should be addressed to E. T. erika.tsingos@cos.uni-heidelberg.de or J. W. jochen.wittbrodt@cos.uni-heidelberg.de.

Figure and Table Legends

Table 1. List of abbreviations used throughout the main text.

Figure 1. Clonal labeling enables analysis of growth patterns in NR and RPE.
(**A**) Schematic anatomy of the fish eye. (**B**) Growth patterns of retinal cell population (concentric rings) and individual clones. (**C**) False color immunostained NR of 3-week old Rx2::^{ERT2}Cre, Gaudí^{RSG} fish with ArCoS and concentric rings of IdU-labelled cells. Overnight IdU pulses were at 1 and 2.5 weeks of age. Leftover undissected autofluorescent tissue fragments cover the far right of the cup-shaped retina. (**D**) Proximal view of clones induced in the NR of Rx2::^{ERT2}Cre, Gaudí$^{2.1}$ fish. Maximum projection of confocal stack of GFP immunostaining in false colors. (**E**) Proximal view of unpigmented lineages induced in the RPE by mosaic bi-allelic knockout of Oca2 using CRISPR/Cas9. Focused projection of brightfield focal stack. Images in (D) and (E) have been rotated to place the optic nerve exit (pink asterisk) ventrally; the embryonic retina is circled with a pink dashed line.

Figure 1 Figure Supplement 1. The retinal radius represents a temporal axis.
(**A**) Photos of newly hatched and young sexually mature adult medaka. The projected area of hatchling and adult eyes is highlighted underneath. (**B**) Schematic drawing of proximal view on clones and IdU “growth rings” of the NR. The central part of the eye is formed embryonically and contains the oldest cells, while the post-embryonic retina is younger and derives from stem cells in the CMZ, which is located at the extreme periphery. The embryonic retina corresponds to the area of the entire differentiated retina in the hatchling; the induction ring corresponds to the position of the CMZ at the timepoint of Cre recombination.

Figure 1 Figure Supplement 2. NR ArCoS form narrow columns spanning all NR layers.
(**A’**) Schematic cross-section of a dissected retina illustrating the various neuronal layers of the NR. The RPE is single-layered. With short fixation times and careful dissection, the RPE and outer nuclear layer can be peeled off from the inner nuclear and ganglion cell layers. (**A’’**) Retina dissected from an adult fish that received a transplant of cells from ubiquitously GFP-expressing donors (Gaudí$^{LoxP\text{-}OUT}$) at embryonic blastula stage. NR clones always span all neuronal layers throughout the retinal radius. Maximum projection of confocal stacks of different preparations of the same retina showing endogenous GFP signal and transmitted light (TL). Pink asterisk marks optic nerve exit. (**B**) Schematic cross-section through an NR ArCoS highlighting clonal columns among differentiated retinal progeny.

Figure 2. Feedback between proliferation and organ growth affects the simulated clonal pattern.
(**A**) Initial condition and properties of the agent-based model of the growing fish retina. Virtual embryonic retina in light green. CMZ cells are assigned unique colors for virtual clonal analysis. (**B’**) Simulated IdU pulse-chase experiment. First pulse: 200-220 h, second pulse: 400-420 h. Screenshot from 435 h. Virtual cells incorporate IdU when they divide and half of the signal is passed on to each daughter cell. (**B’’**) Cell age (hours elapsed since last cell division) form a gradient with the oldest cells in the virtual embryonic retina. (**C’**) In the inducer growth mode, the modelled tissue signals upstream to drive growth of other tissues in the organ. (**C’’**) Representative screenshot of inducer growth mode. (**C’’’**) Sample of 10 clones from (C’’). Colors: ratio of full perimeter by bounding rectangle perimeter, a metric for shape complexity. (**C’’’’**) Cell division intervals plotted against the mean average overlap. (**D’**) In the responder growth mode, control of the growth of the modelled tissue is downstream of an external signal. (**D’’**) Representative screenshot of the responder growth mode. (**D’’’**) Sample of 10 clones from (D’’) evaluated by the same shape metric as in (C’’’). (**D’’’’**) Cell division intervals plotted against the mean average overlap. Note the higher range of values for cells over the threshold overlap of 0.2.

Video 1. The simulated retina is always densely covered by cells.
Simulation of the responder growth mode illustrating clonal lineage formation while the virtual eye grows. When cells divide they briefly flash white.

Video 2. Lateral view of a simulation of the inducer growth mode.
Simulation of the inducer growth mode illustrating clonal lineage formation while the virtual eye grows. When cells divide they briefly flash white.

Figure 2 Figure Supplement 1. Process diagram summarizing model decision tree.
(**A**) At every simulation step, the biomechanical model is solved followed by simulation of the cell behavioral model. Green shaded steps expanded in (B). (**B**) Summary of cell behavioral decision tree. If a cell decides to divide but the minimum cell cycle time has not elapsed, it will suppress division and check only the other conditions (proliferative cell type, permissive overlap, minimum time elapsed).

Figure 2 Figure Supplement 2. Cell position update with radial growth of the simulated retina.
To simulate radial growth, the vectors extending from the eye globe's center to the cells' center are extended to match the radius of the growing hemispherical organ. This leads to a decrease in cell density over time as described for growing fish eyes (Lyall, 1957; Johns, 1977; Ohki and Aoki, 1985). Additionally, every numerical step of the solver for the biomechanical force-balance includes similar repositioning of all cells, to ensure they stay on the hemispherical surface. Each simulation step includes 100 such iterations.

Figure 2 Figure Supplement 3. Obstacle cells create an impassable boundary at the hemisphere's edge.
A single layer of tightly packed cells prevents cell movement beyond the hemispherical edge. These obstacle cells represent the edge of the tissue and have no other influence on the simulation.

Figure 3. Cell division variability is lower in NR and inducer growth mode, higher in RPE and responder growth mode.
(**A'-A''**) Proximal view of segmented patches in adult NR and RPE and simulated patches in inducer and responder growth mode. The central (virtual) embryonic retina was excluded from analysis. (**B**) Different degrees of variability in cell division timing affect the clone pattern. (**C'-C''**) Upper panels: Superposition of labelled patches in the NR (n=156 patches from 7 retinae), RPE (n=142 patches from 10 retinae), inducer growth mode (n=145 patches from 5 simulations), and responder growth mode (n=107 patches from 5 simulations). The radius was normalized to the same length in all samples. Lower panels: Gaussian fits of normalized pixel intensity profiles projected along the vertical axis. σ - Standard deviation of fit. (**D**) Distribution of number of nodes of skeletonized patches. Inset: Examples of patches without nodes (I), with only 1 node (II), or with multiple nodes (III). (**E**) Rug plot showing number of patches that are not connected to the embryonic retina ("late arising patches") at the respective positions along the normalized radius. NR (n = 54 late patches) and inducer growth mode (n = 35 late patches) display a marked peak in the central portion, while RPE (n = 56 late patches) and responder growth mode (n = 37 late patches) have a more uniform distribution.

Video 3. Simulation where 20% of stem cells were labeled in white showing clone fusion and fragmentation.
Cells that were initially differentiated are shown in light gray. When cells divide they briefly flash white.

Figure 3 Figure Supplement 1. Relationship between clones, patches, and polyclones.
The term clone denotes lineages derived from a single founder cell, while polyclones are conglomerates of clones that are spatially clustered. We define patches as contiguous domains of labelled cells regardless of their clonal relationship. A patch may represent a clone, a fragment of a clone, or a polyclone.

Figure 3 Figure Supplement 2. Distributions of patch width and length in experiment and simulation
(**A**) Distribution of maximum width of patches that span at least 20% of the radial coordinate. (**B**) Distribution of maximum patch length normalized against the postembryonic retinal radius; late arising patches (central-most pixel after 20% of the radius) were excluded from the analysis. Note the bimodal distribution that results from the

abundance of very short and very long patches. (**C**) Illustration of a retina before and after transforming from polar coordinates centered on the embryonic retina to a cartesian representation. Patch bordered in dotted red line is magnified on the right to illustrate the metrics used for plotting distributions in (A) and (B) of this figure.

Figure 4. The majority of stem cells differentiates due to cell competition for niche space.
(**A'**) Detail of inducer growth mode simulation where clone label was initiated at a radius of R=100 µm. Small clusters lie centrally, while virtual ArCoS start peripherally. Two virtual ArCoS are highlighted. Pink dashed lines encircle virtual induction ring. (**A''**) Same simulation as in (A'), but with clone label initiated at R=150 µm. The second wave of clonal label leads to a renewed occurrence of small clusters. Two polyclonal patches are highlighted, which correspond to subclones of the highlighted clones in (A'). (**B**) The majority of virtual ArCoS derives from stem cells that in simulation step 0 were located in the two most peripheral rows of the virtual CMZ. (**C'**) Proximal view of NR clones. (**C''**) Magnification of central retina from (C'). (C'-C'') Maximum projection of confocal stack of GFP signal in false colors; rotated to place optic nerve exit (pink asterisk) ventrally. (**D'**) Proximal view of simulated clones. (**D''**) Magnification of central retina from (D'). (C'-D') Retinal edge marked by white dashed circle; dashed pink lines encircle and subdivide induction ring into central and peripheral parts; pink arrowheads mark ArCoS, yellow arrowheads mark terminated clones. (**E**) Scheme of the experiment. (**F**) Proportions of ArCoS and terminated clones arising from central and peripheral induction ring in experiment (n = 20 retinae) and simulation (n = 5 simulations, sampled 6 times each). p-values calculated with a 2-sample test for equality of proportions.

Video 4. A terminated clone and an ArCoS originating from the peripheral-most stem cell row.
Simulation of the inducer growth mode. Two cells are highlighted in the first simulation step: A purple cell that will give rise to an ArCoS (purple circle), and a green cell that will divide only a few times before its lineage completely exits the niche, forming a terminated clone (green circle). Note how almost all proliferative cells not at the very edge of the hemisphere are pushed out of the proliferative domain and form terminated clones.

Figure 4 Figure Supplement 1. Induction ring in very sparsely labelled samples.
(**A-B**) Proximal view of NR clones. If label is very sparse, clones occur almost exclusively in the induction ring, with very few or no ArCoS at all, showing that the majority of Rx2-expressing cells form terminated clones. Maximum projection of confocal stack of GFP signal in false colors; rotated to position the optic nerve exit (pink asterisk) ventrally. (**C-D**) Sparse labelling in simulations. Pink dashed lines encircle induction ring, retinal margin marked by white dashed line.

Figure 5. NR stem cells undergo predominant radial divisions as predicted for a shape-giving function.
(**A**) If organ shape is imposed externally, then cells in the tissue will distribute to fill the available space. Regardless of cell division axes, organ geometry will lead to a directional growth in stripes. (**B'**) If organ shape is regulated by cell division axes, then oriented divisions are required. (**B''**) If the NR regulates shape through cell divisions, then more divisions along the radial axis are needed to maintain hemispherical geometry. (**C'-C'''**) Examples of experimental and simulated data. For simulations, the full clone population and a random sample are shown. The initial model label was induced at R=150 µm to match the experimental induction radius. Scale bars: 200 µm. (**D'**) Mean clone width (solid lines) and 95% confidence intervals (shaded) plotted along the post-embryonic retinal radius. Experimental data: n = 99 ArCoS across 7 retinae. Simulation, random division axis: n = 102 ArCoS from 5 simulations; ideal division axis: n = 133 ArCoS from 5 simulations. p values were calculated with Welch two sample t-test. (**D''**) Schematic of radial compartments of the NR and measurements of clone width in proximal view. The clone width plotted in D' corresponds to the angle enclosed by the clone borders at every radial position.

Figure 5 Figure Supplement 1. Average clone width increases with increasing circumferential divisions

(**A'-A'''**) Example simulations where the probability for circumferential divisions was set to a fixed value of 50% (A'), 25% (A''), and 0% (A'''). (**B**) Average clone width along the post-embryonic radius for circumferential division probability ranging from 0% to 50% (one simulation each).

Figure 6. Stem cells in the ventral CMZ have different proliferation parameters.
(**A'**) Proximal view of NR clones highlighting the discrepancy between retinal center and embryonic retinal center. Depicted sample is the same as in Figure 1 D. (**A''**) A differential proliferative behavior along the CMZ circumference can explain the shift in position of the embryonic retina. (**B'-B''''**) Simulations where lineages whose embryonic origin is in the ventral sector inherit a signal that leads to different proliferation parameters. A shift occurred when ventral lineages had both lower division probability and circumferential divisions. Clones originating in ventral embryonic CMZ are outlined in red. (**C'-C''''**) Simulations where all cells in a ventral 90° sector exhibit different proliferation parameters regardless of lineage relationships. A shift occurred in conditions with slower proliferation as well as slower proliferation combined with circumferential division axis bias. (**D'-E''''**) Patch superposition for experimental data as well as the three simulated conditions that display a ventral shift of the embryonic retina. (D'-D'''') Non-ventral patches. (E'-E'''') Ventral patches.

Figure 6 Figure Supplement 1. Magnification of simulations displaying a ventral shift
(**A**) Magnification of Figure 6 B''''. White arrowheads highlight unusually shaped clones with lateral interdigitations. (**B**) Magnification of Figure 6 C'''. White arrowheads highlight unusually shaped clones that overexpand circumferentially and bend towards the ventral side. (**C**) Magnification of Figure 6 C''''. None of the clones display obvious deviations from the average. (**D'-D''''**) Distribution of maximum width of patches that span at least 20% of the radial coordinate.

Figure 6 Figure Supplement 2. Definition of the ventral sector in the simulation.
(**A-B**) Schematic side and proximal view showing values used in Figure Appendix 1-equations 16-17 to calculate which cells are located in the ventral sector. For each cell, the corresponding small circle radius R_{small} is calculated. This cell is assigned to the ventral sector if it lies within the red shaded region in (B). (**C-D**) Corresponding views in simulation screenshots showing cells in red that satisfy Figure Appendix 1-equations 16 and 17.

Figure 7. Summary of results and proposed model of CMZ dynamics
(**A**) Growth coordination of NR and RPE is achieved by the NR providing instructive stimuli that modulate proliferation of RPE stem cells. As a result of the different growth strategies, variability in cell division timing is elevated in the RPE and lowered in the NR. (**B**) A base level of variability persists in the NR, such that individual stem cells may differentiate and some multipotent progenitor cells drift to a stem cell fate according to a spatially biased neutral drift model. Thus, stem cells and multipotent progenitor cells have identical proliferative potency. (**C**) Schematic summary of findings and proposed model, where different NR cell proliferation parameters affect both global and local retinal properties.

Source Data Legends

Figure 3-source data 1 - Patch outlines

Figure 3 C'-C'') "roi" format files of aligned individual patch outlines for each condition. Data can be opened in the program "ImageJ".

Figure 3-source data 2 – Patch superposition

Figure 3 C'-C'') "Tif" format files of patch superposition, which can be opened in the program "ImageJ". Averaged pixel intensity profiles measured on the patch superposition in ImageJ using the "Plot Profile" function over a rectangle encompassing the entire image.

Figure 3-source data 3 – Nodes per patch

Figure 3 D) Counts of number of nodes in each patch for each condition.

Figure 3-source data 4 – Late arising patches

Figure 3 E) Counts of number of patches along normalized radial bins. For each patch, the starting position along normalized radial bins was noted. Patches that did not begin in the first radial bin (and thus were not connected to the central embryonic retina) were considered "late arising patches".

Figure 3-source data 5 – Patch width distribution

Figure 3-supplement 2 A) Maximum patch width in pixels for each condition.

Figure 3-source data 6 – Patch height distribution

Figure 3-supplement 2 B) Maximum patch height (expressed as percent of total postembryonic radius) for each condition.

Figure 3-source data 7. Comparison of variances of maximum patch width distribution.

F-test of equality of variance applied to the data in Figure 3 Figure Supplement 2 A rounded to two digits.

Figure 3-source data 8. Comparison of distribution of number of nodes.

Wilcoxon rank sum test applied to the data in Figure 3 D rounded to two digits.

Figure 3-source data 9. Comparison of distribution of late arising patches.

Wilcoxon rank sum test applied to the data in Figure 3 E rounded to two digits.

Figure 4-source data 1 – Origin of ArCoS and terminated clones in the simulation

Figure 4 B) ArCoS were defined as clones that still retained cells in the virtual CMZ at the final simulation step used for analysis, i.e. when the virtual retina had attained a radius of R = 800 µm. All other clones counted as terminated clones. The initial position at simulation step 0 of the founder stem cells for each clone was extracted from the simulated data and assigned to a 5 µm-wide bin corresponding to each of the cell rows in the virtual CMZ.

Figure 4-source data 2 – Proportion of ArCoS and terminated clones in induction ring zones

Figure 4 F) Counts of ArCoS and terminated clones originating in the central and peripheral induction ring. Data were quantified manually; experimental data consisted of 20 retinae from 10 fish; simulated data consisted of 5 simulations, each sampled 6 times. The position of the induction ring was

estimated based on the following criteria: The inner circle was placed such that it enclosed as many 1-cell clones as possible (*i.e.* labelled differentiated cells in the experimental data). The outer circle was placed such that it enclosed all few-cell clusters and crossed all ArCoS. The induction circle was split in the middle and each clone was assigned to the central-most or peripheral-most ring based on the position of its central-most pixel.

Figure 5-source data 1 – Mean and 95% confidence interval of clone width

Figure 5 D') Position along the radius (in µm), mean clone angle (expressed as percent of 360°), and 95% confidence interval for experimental and simulated data.

Figure 5-source data 2 – Clone width in simulations with varying circumferential bias

Figure 5-figure supplement 1 B) Position along the radius (in µm) and mean clone angle (expressed as percent of 360°) for simulated data. Data were obtained for 1 simulation for each condition.

Figure 6-source data 1 – Patch outlines

Figure 6 D'-E'''') "roi" format files of aligned individual patch outlines for each condition. Data can be opened in the program "ImageJ".

Figure 6-source data 2 – Patch width distribution

Figure 6-figure supplement 1 D'-D'''') Maximum patch width in pixels for each condition. Experimental data are the same as NR data used in Figure 3, but split among ventral and non-ventral patches. For simulated data, the measurements were done on multiple samples from 3 simulations each.

Source Code Legend

Source Code 1 - EPISIM Simulator implementation of model described in Appendix 1

Excerpt of the relevant parts of EPISIM Simulator source code. The full source code is available at https://gitlab.com/EPISIM/EPISIM-Simulator (Sütterlin 2019).

Supplementary Files Legend

Supplementary File 1 - EPISIM Simulator executable model file

Compiled model file that can be opened in EPISIM Simulator to simulate the model described in this work.

Supplementary File 2 - EPISIM Model project archive

Model project file that can be imported in EPISIM Modeller to visualize the cell behavioral logic implemented in the model described in this work.

Supplementary File 3 - Instructions for using supplementary model files

Step by step instructions on how to open Supplementary File 1 and Supplementary File 2.

Tables and figures

Table 1. List of abbreviations used throughout the main text. NR	neural retina
RPE	retinal pigment epithelium
CMZ	ciliary marginal zone
Rx2	retina-specific homeobox gene 2
ArCoS	arched continuous stripes
GFP	green fluorescent protein
Oca2	oculo-cutaneous albinism 2
IdU	5-Iodo-2′-deoxyuridine

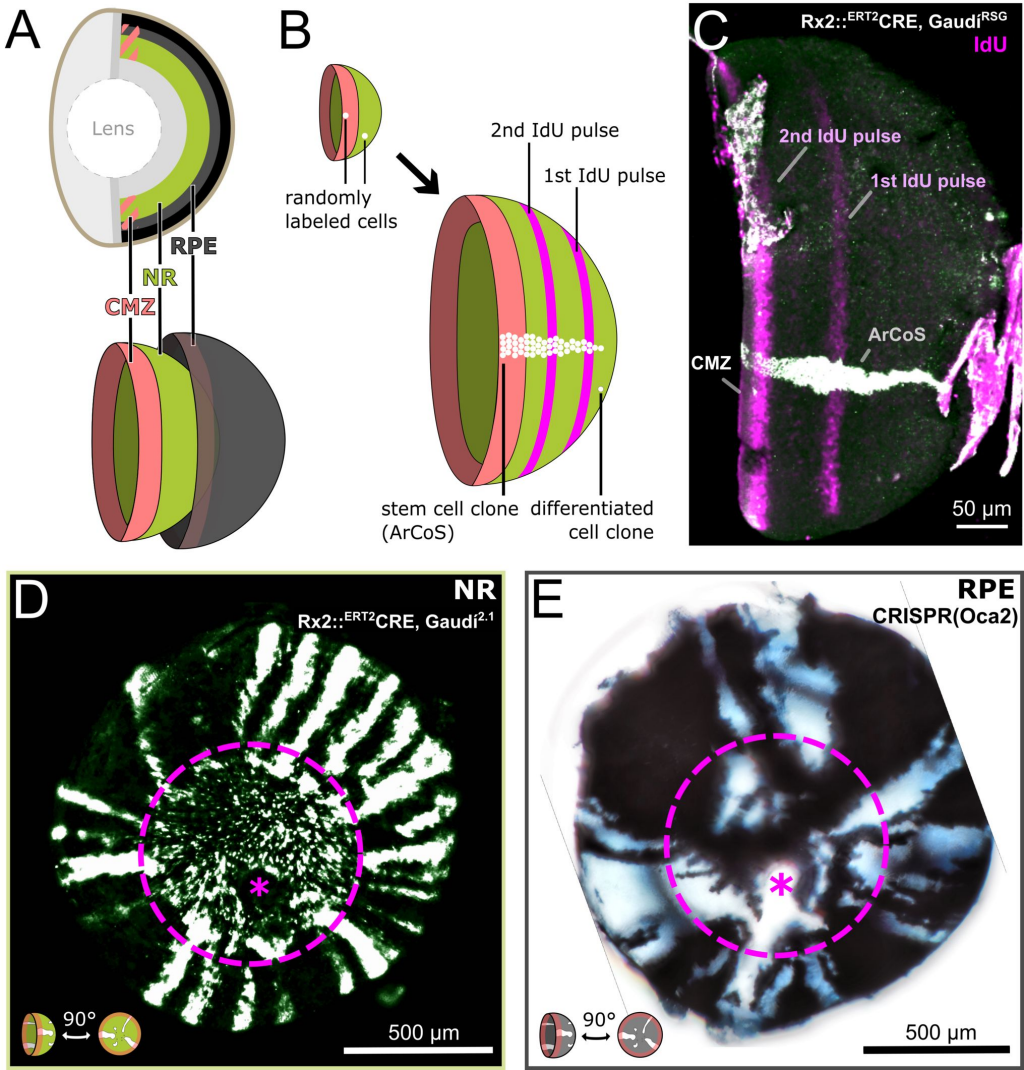
A
Lens
RPE
NR
CMZ
B
randomly
labeled cells
2nd IdU pulse
1st IdU pulse
stem cell clone
(ArCoS)
differentiated
cell clone
C
Rx2::ERT2CRE, GaudíRSG
IdU
2nd IdU pulse
1st IdU pulse
ArCoS
CMZ
50 µm
D
NR
Rx2::ERT2CRE, Gaudí2.1
90°
500 µm
E
RPE
CRISPR(Oca2)
90°
500 µm

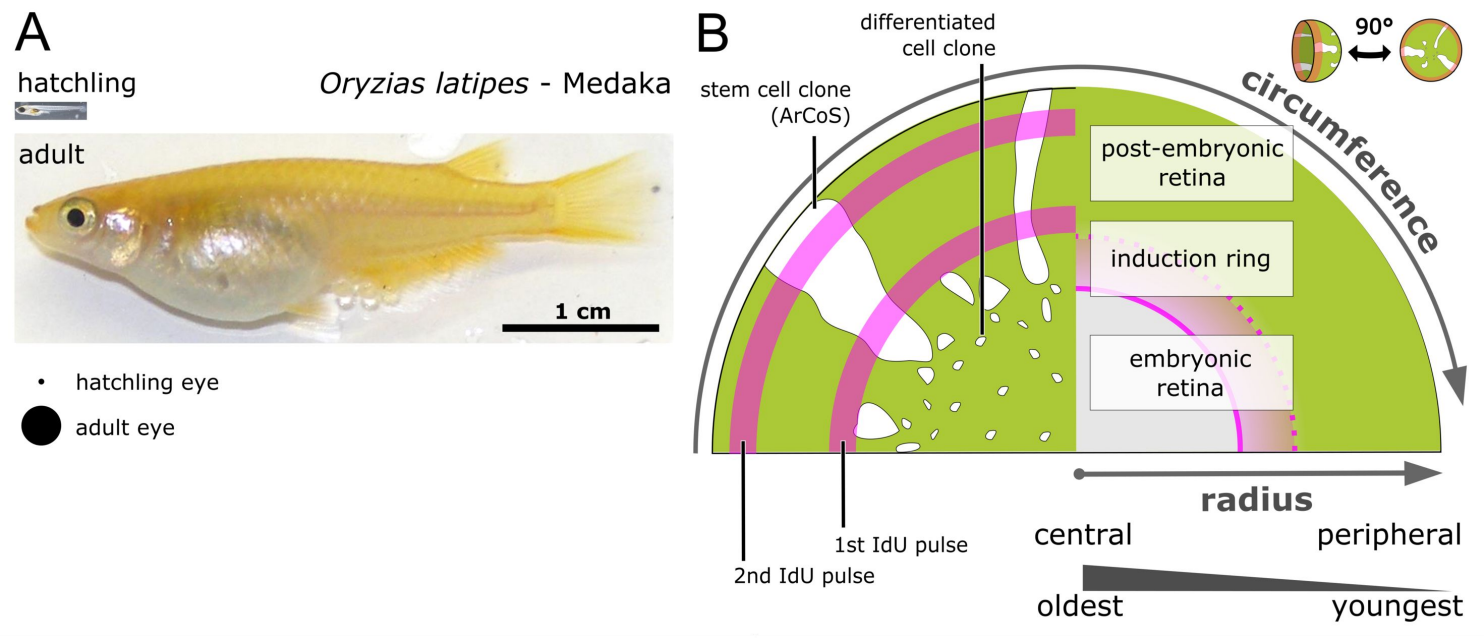
A
hatchling
Oryzias latipes - Medaka
adult
1 cm
hatchling eye
adult eye
B
differentiated cell clone
stem cell clone (ArCoS)
90°
circumference
post-embryonic retina
induction ring
embryonic retina
radius
central
peripheral
1st IdU pulse
2nd IdU pulse
oldest
youngest

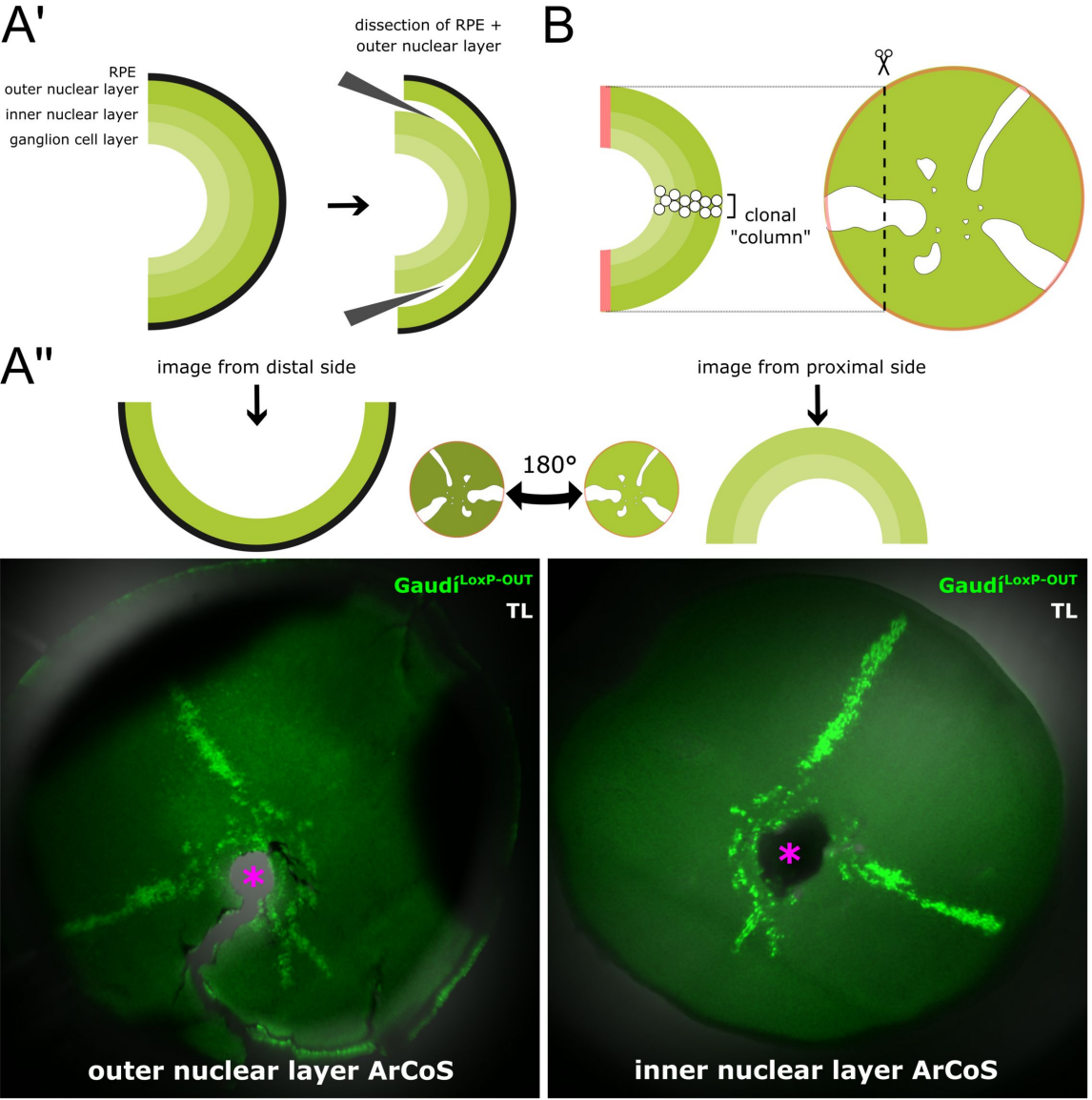

Tsingos et al. Figure 1 Supplement 2

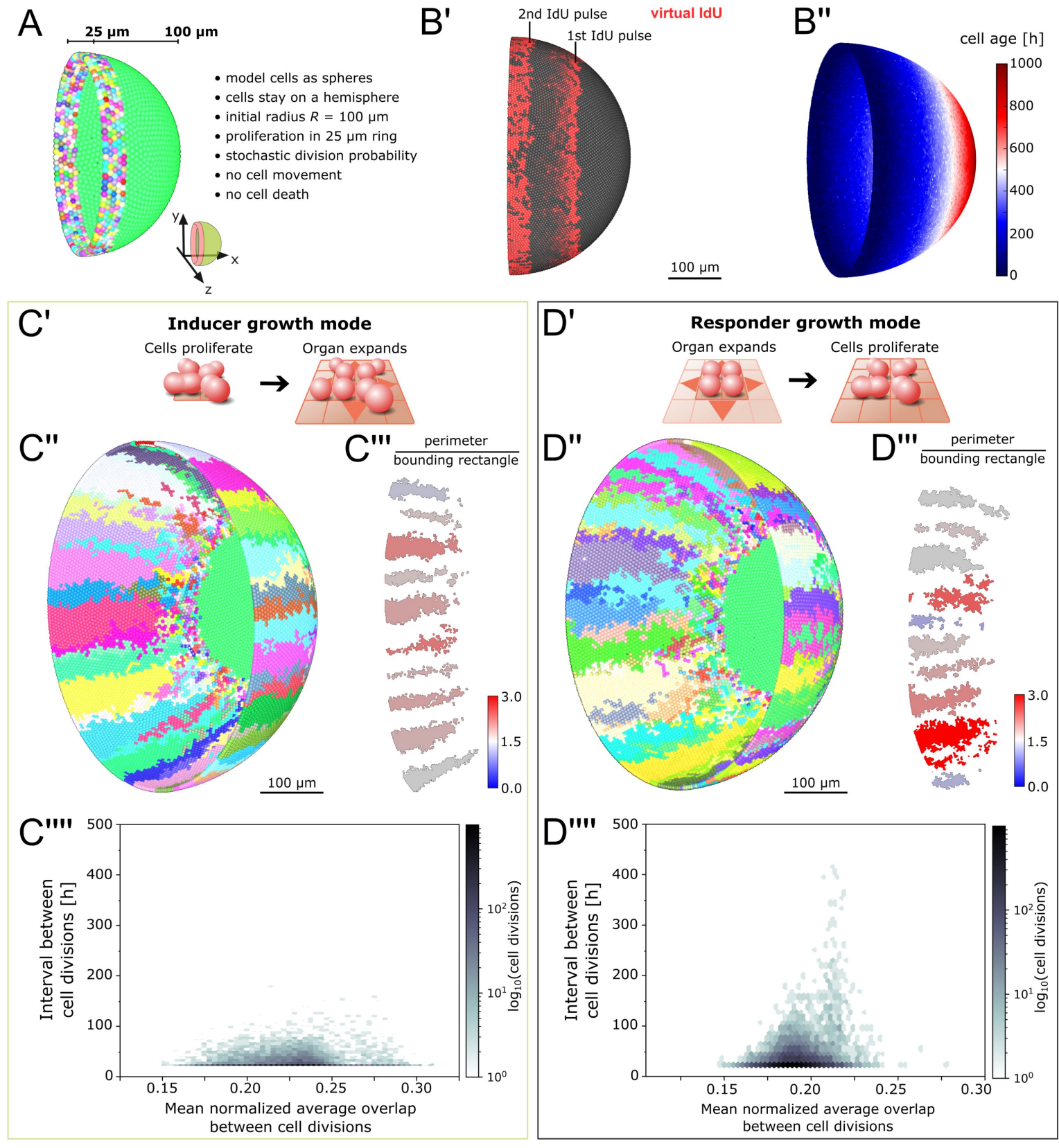
A
25 µm
100 µm
• model cells as spheres
• cells stay on a hemisphere
• initial radius R = 100 µm
• proliferation in 25 µm ring
• stochastic division probability
• no cell movement
• no cell death
y
x
z
B'
2nd IdU pulse
1st IdU pulse
virtual IdU
100 µm
B''
cell age [h]
1000
800
600
400
200
0
C'
Inducer growth mode
Cells proliferate
Organ expands
C''
100 µm
C'''
perimeter
bounding rectangle
3.0
1.5
0.0
C''''
Interval between cell divisions [h]
500
400
300
200
100
0
0.15
0.20
0.25
0.30
Mean normalized average overlap between cell divisions
log10(cell divisions)
10^2
10^1
10^0
D'
Responder growth mode
Organ expands
Cells proliferate
D''
100 µm
D'''
perimeter
bounding rectangle
3.0
1.5
0.0
D''''
Interval between cell divisions [h]
500
400
300
200
100
0
0.15
0.20
0.25
0.30
Mean normalized average overlap between cell divisions
log10(cell divisions)
10^2
10^1
10^0

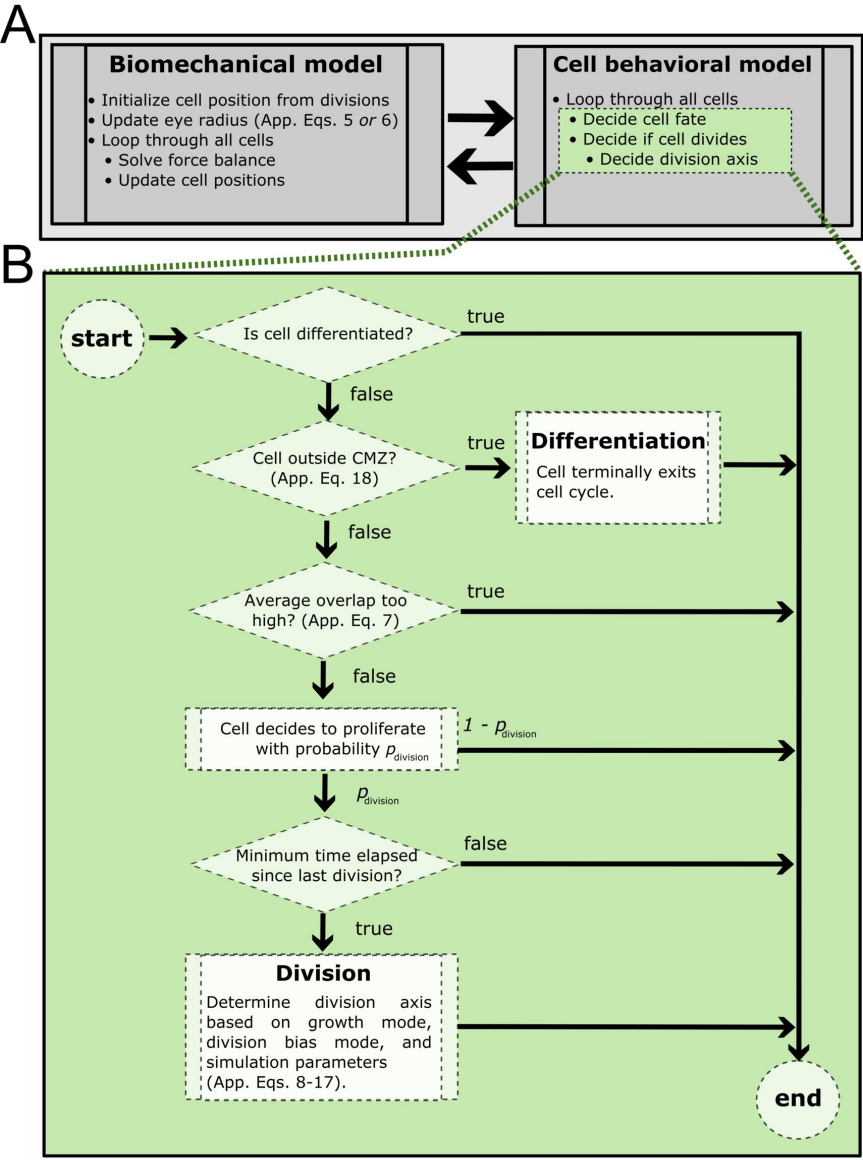

Tsingos et al. Figure 2 Supplement 1

Cell position update with radial growth

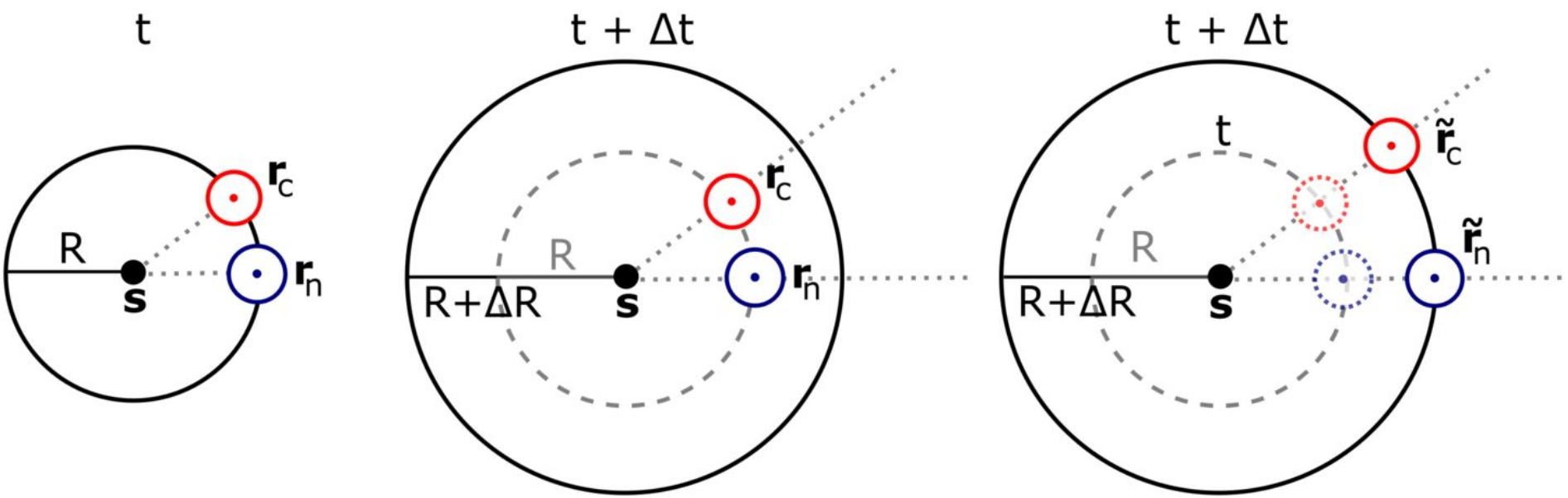

1. Obtain new radius R+ΔR (App. Eq. 5 [inducer growth mode] *or* 6 [responder growth mode]).
2. Extend cell position vector to match new radius (App. Eq. 4)
3. Calculate biomechanical force balance.

Tsingos et al. Figure 2 Supplement 2

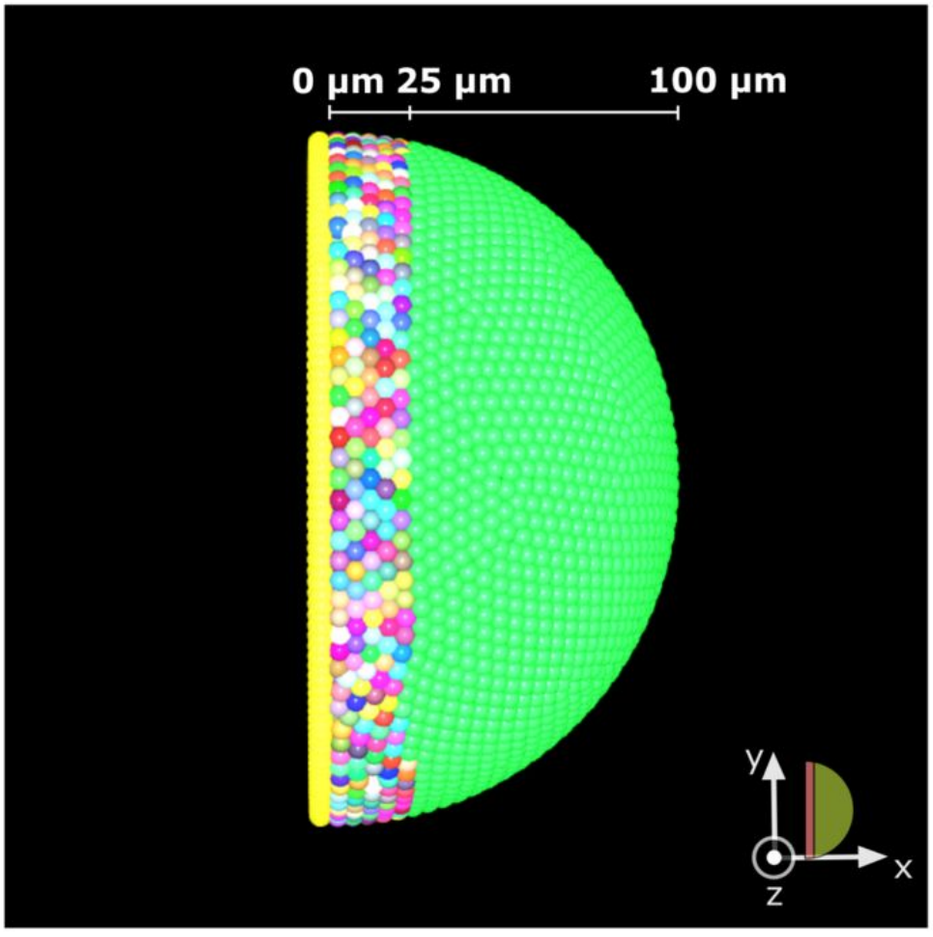
0 µm 25 µm
100 µm
y
x
z

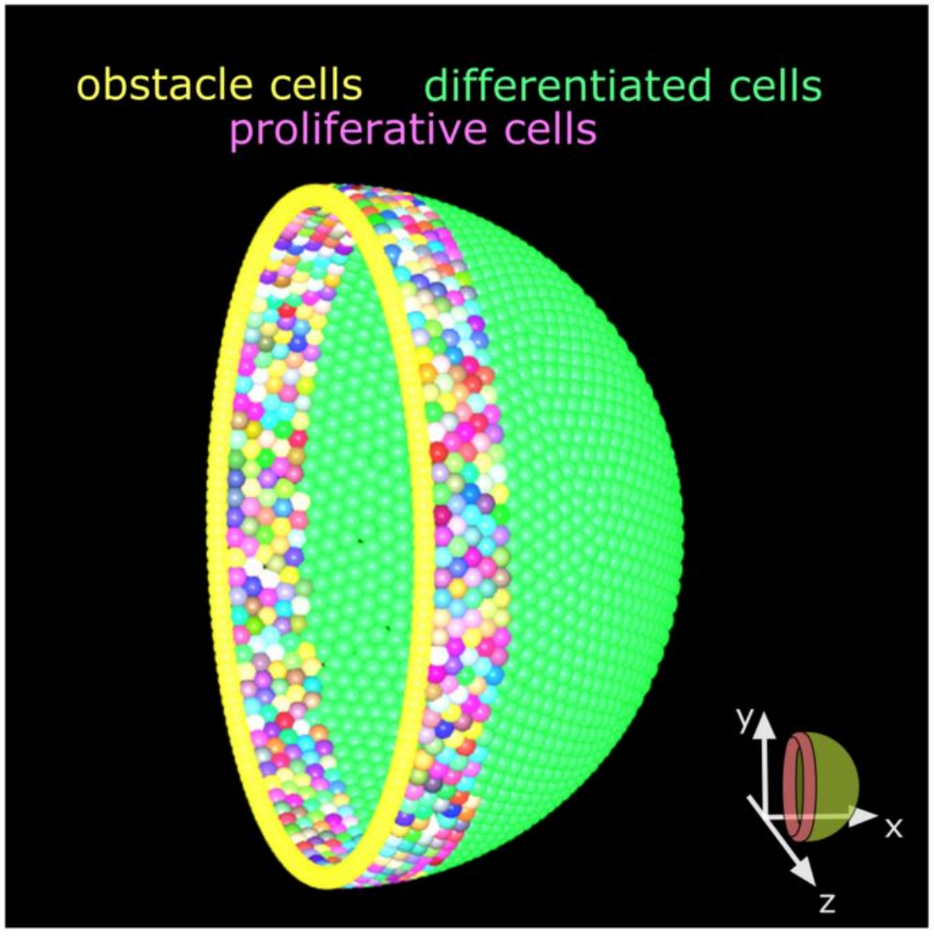
obstacle cells
differentiated cells
proliferative cells
y
x
z

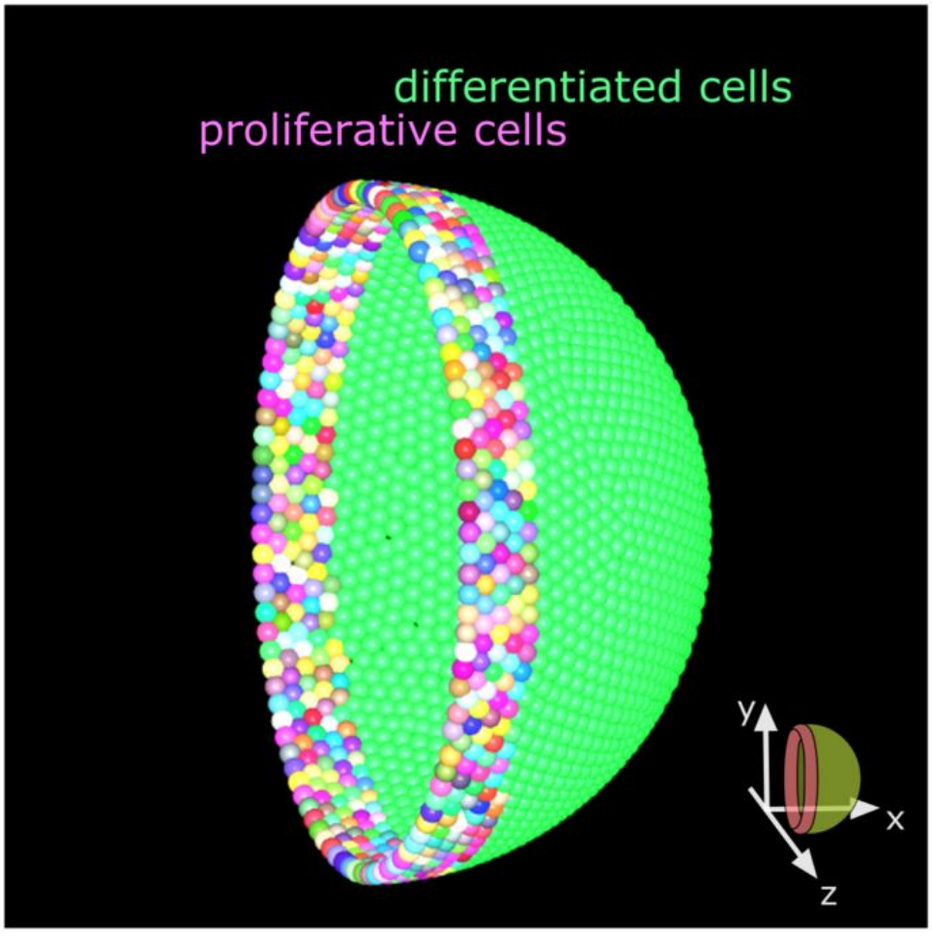
differentiated cells
proliferative cells
y
x
z

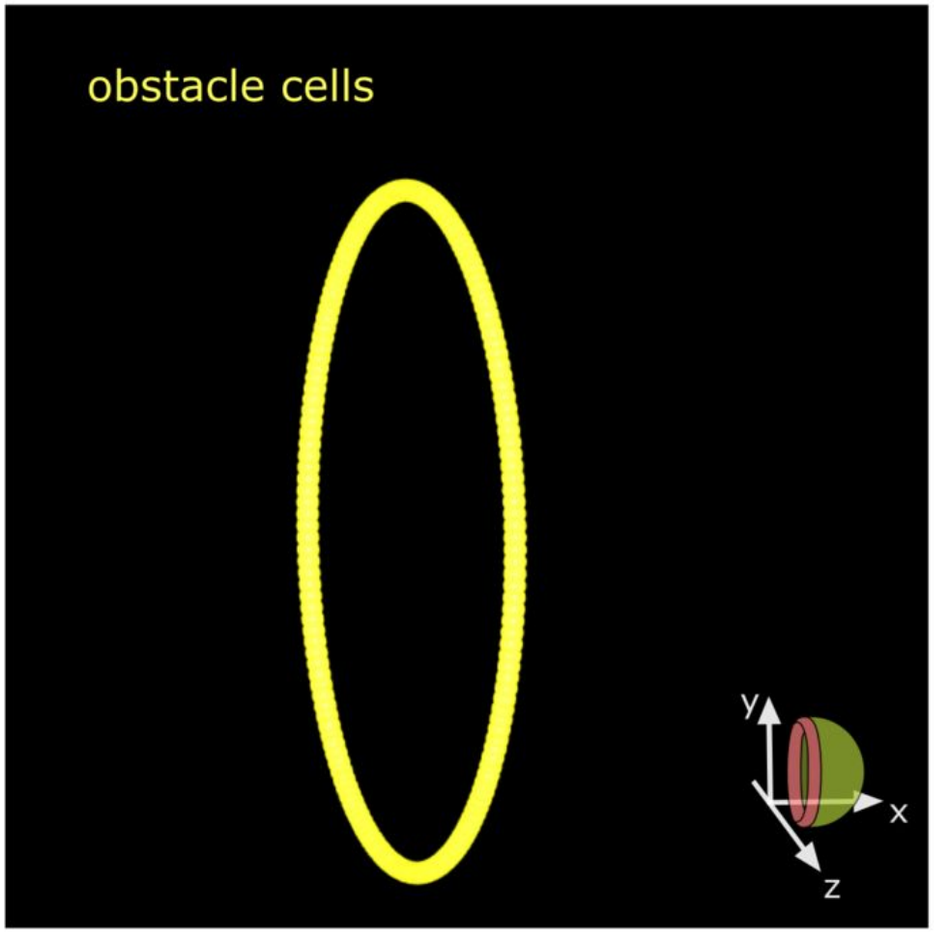
obstacle cells
y
x
z

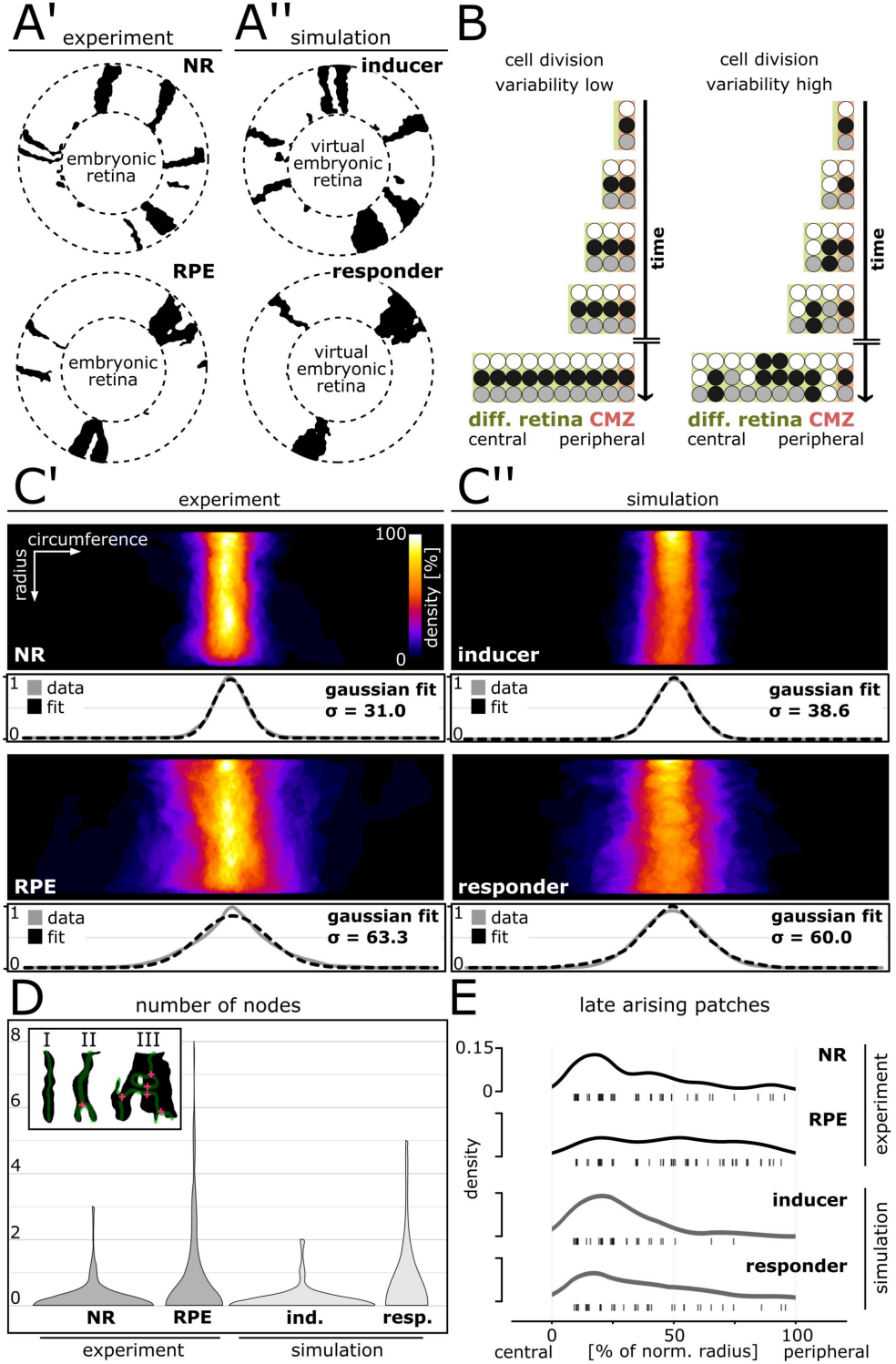
A'
experiment
A''
simulation
NR
embryonic retina
RPE
embryonic retina
inducer
virtual embryonic retina
responder
virtual embryonic retina
B
cell division variability low
cell division variability high
time
time
diff. retina CMZ
central
peripheral
diff. retina CMZ
central
peripheral
C'
experiment
C''
simulation
circumference
radius
100
density [%]
0
NR
data
fit
gaussian fit
σ = 31.0
inducer
data
fit
gaussian fit
σ = 38.6
RPE
data
fit
gaussian fit
σ = 63.3
responder
data
fit
gaussian fit
σ = 60.0
D
number of nodes
I
II
III
NR
RPE
ind.
resp.
experiment
simulation
E
late arising patches
density
NR
RPE
inducer
responder
experiment
simulation
central
[% of norm. radius]
peripheral

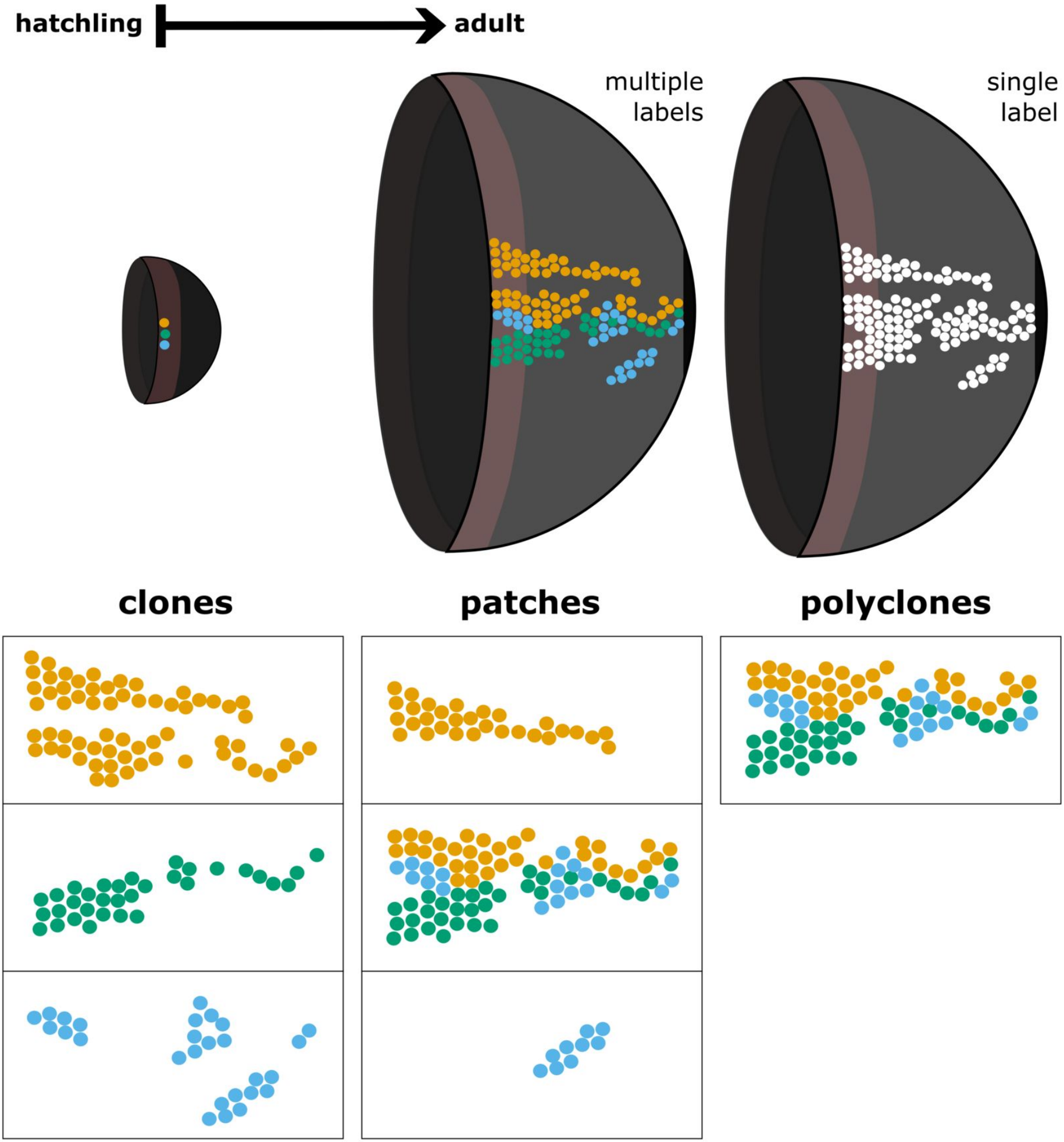
hatchling
adult
multiple labels
single label
clones
patches
polyclones

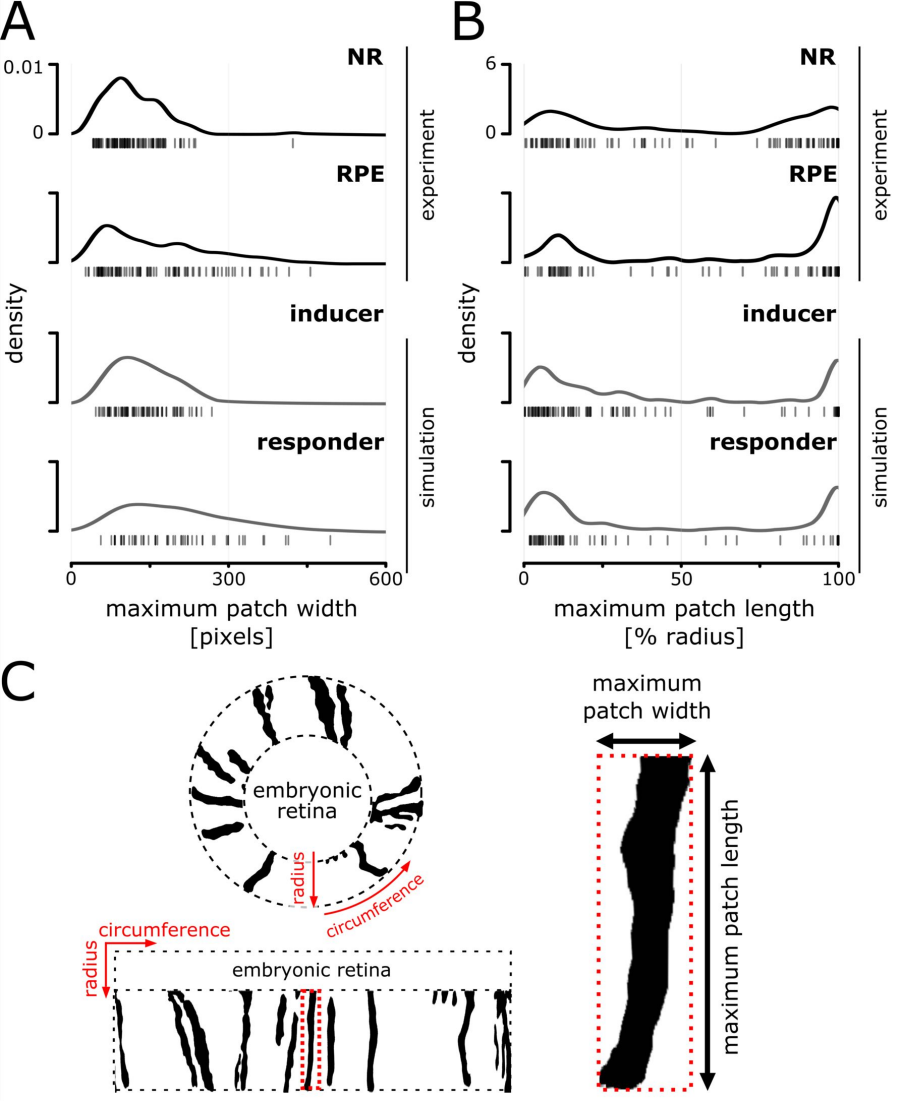
A
B
C
NR
RPE
inducer
responder
experiment
simulation
density
0.01
0
6
0
0
300
600
0
50
100
maximum patch width
[pixels]
maximum patch length
[% radius]
embryonic retina
radius
circumference
circumference
radius
embryonic retina
maximum
patch width
maximum patch length

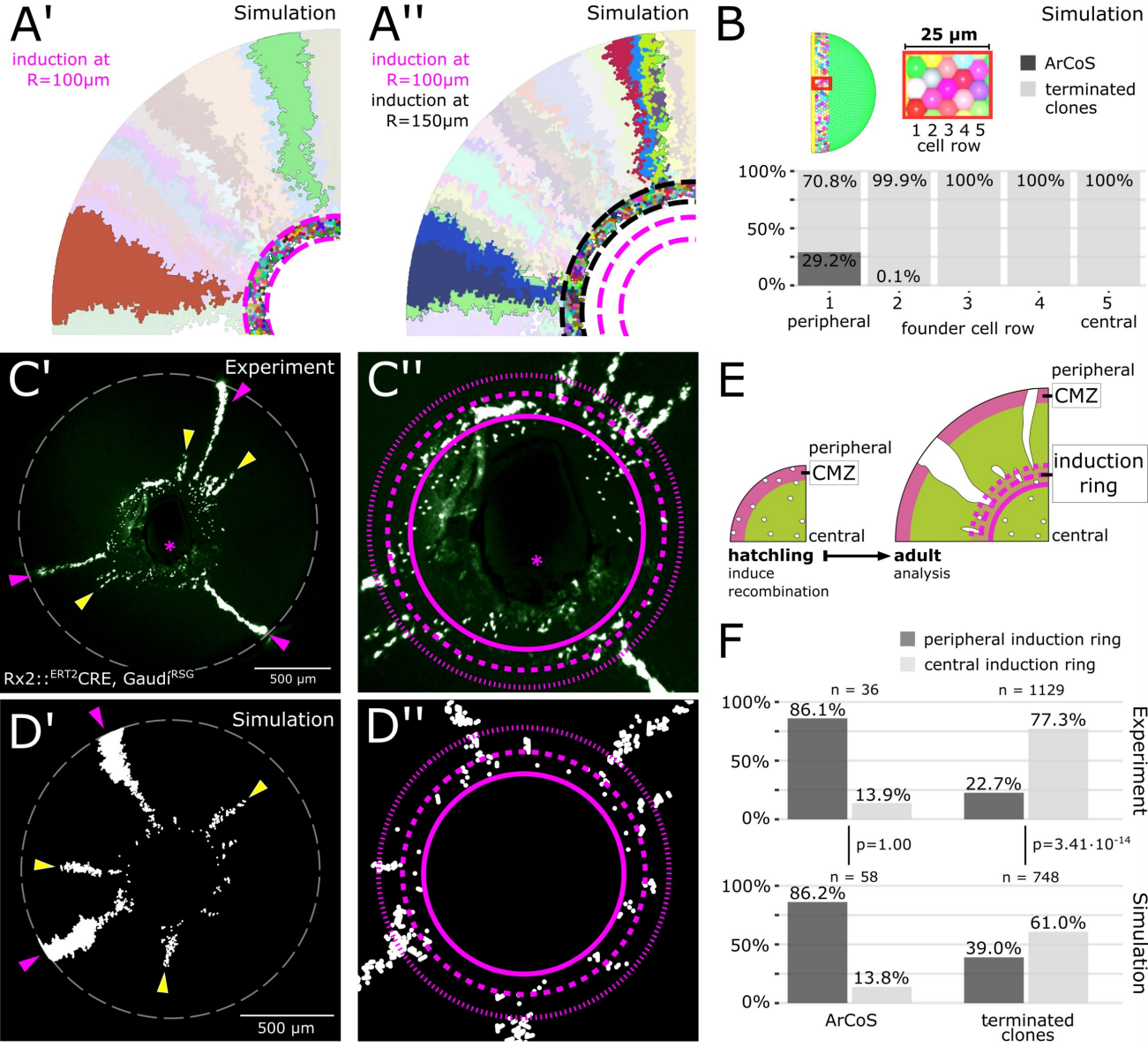
A'
Simulation
induction at R=100µm
A''
Simulation
induction at R=100µm
induction at R=150µm
B
Simulation
25 µm
1 2 3 4 5
cell row
ArCoS
terminated clones
100%
50%
0%
70.8%
99.9%
100%
100%
100%
29.2%
0.1%
1
2
3
4
5
peripheral
founder cell row
central
C'
Experiment
Rx2::ERT2CRE, GaudíRSG
500 µm
C''
D'
Simulation
500 µm
D''
E
peripheral
CMZ
central
hatchling
induce recombination
adult
analysis
peripheral
CMZ
induction ring
central
F
peripheral induction ring
central induction ring
n = 36
n = 1129
86.1%
13.9%
22.7%
77.3%
Experiment
p=1.00
p=3.41·10-14
n = 58
n = 748
86.2%
13.8%
39.0%
61.0%
Simulation
ArCoS
terminated clones

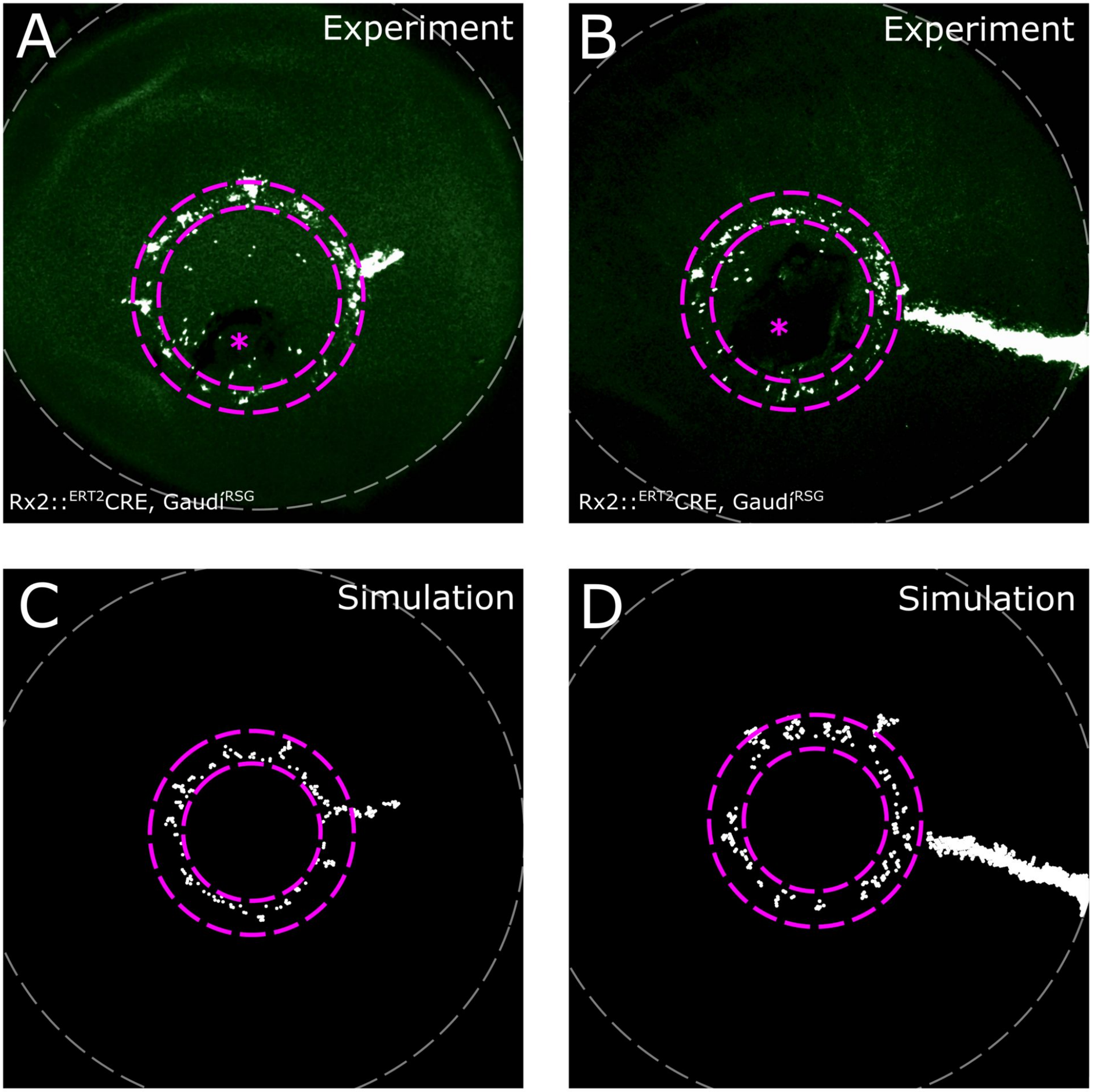
A
Experiment
Rx2::ERT2CRE, GaudíRSG
B
Experiment
Rx2::ERT2CRE, GaudíRSG
C
Simulation
D
Simulation

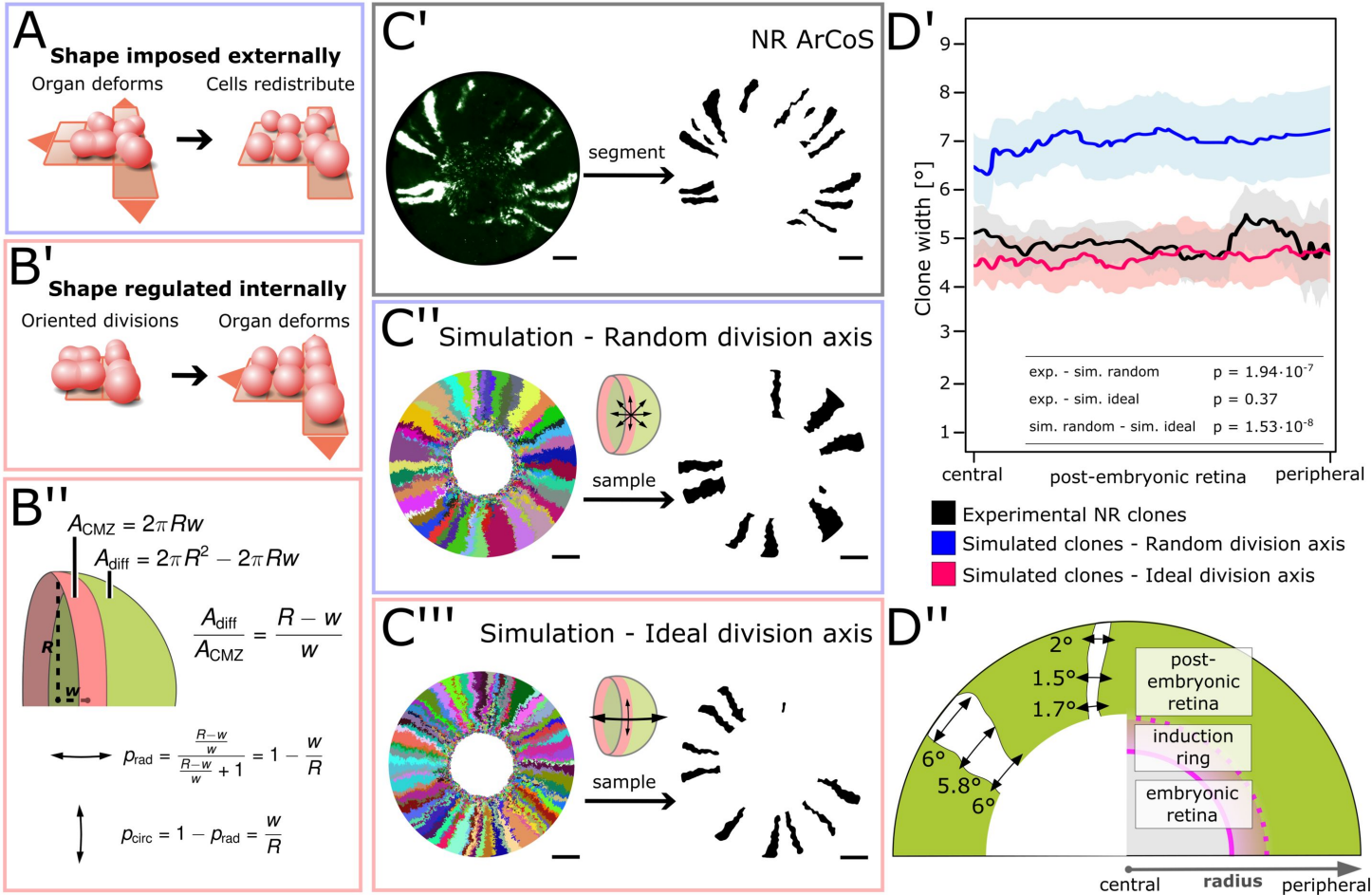
A
Shape imposed externally
Organ deforms
Cells redistribute
B'
Shape regulated internally
Oriented divisions
Organ deforms
B''
$A_{CMZ} = 2\pi Rw$
$A_{diff} = 2\pi R^2 - 2\pi Rw$
R
w
$\frac{A_{diff}}{A_{CMZ}} = \frac{R-w}{w}$
$p_{rad} = \frac{\frac{R-w}{w}}{\frac{R-w}{w}+1} = 1 - \frac{w}{R}$
$p_{circ} = 1 - p_{rad} = \frac{w}{R}$
C'
NR ArCoS
segment
C''
Simulation - Random division axis
sample
C'''
Simulation - Ideal division axis
sample
D'
Clone width [°]
1
2
3
4
5
6
7
8
9
exp. - sim. random p = 1.94·10^-7
exp. - sim. ideal p = 0.37
sim. random - sim. ideal p = 1.53·10^-8
central
post-embryonic retina
peripheral
Experimental NR clones
Simulated clones - Random division axis
Simulated clones - Ideal division axis
D''
2°
1.5°
1.7°
6°
5.8°
6°
post-embryonic retina
induction ring
embryonic retina
central
radius
peripheral

A'

Simulation - p_{circ} = 0.50

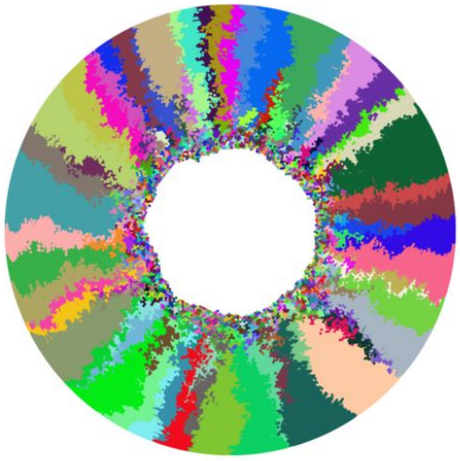

A''

Simulation - p_{circ} = 0.25

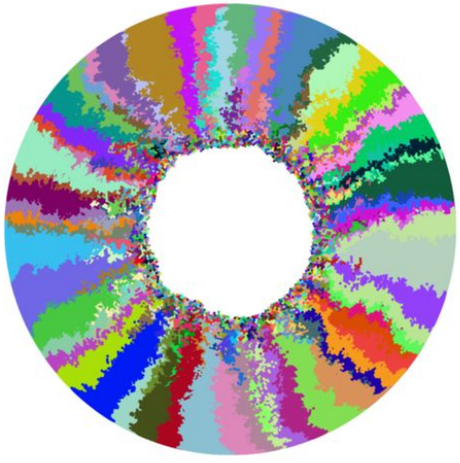

A'''

Simulation - p_{circ} = 0.00

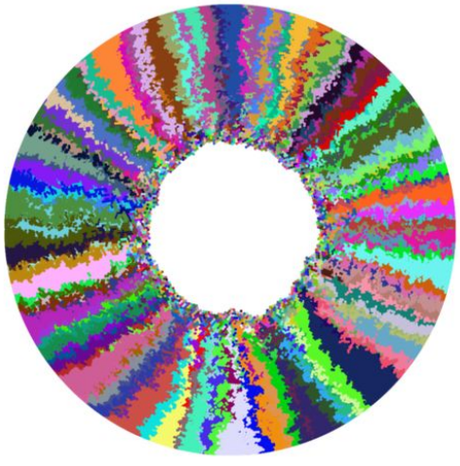

B

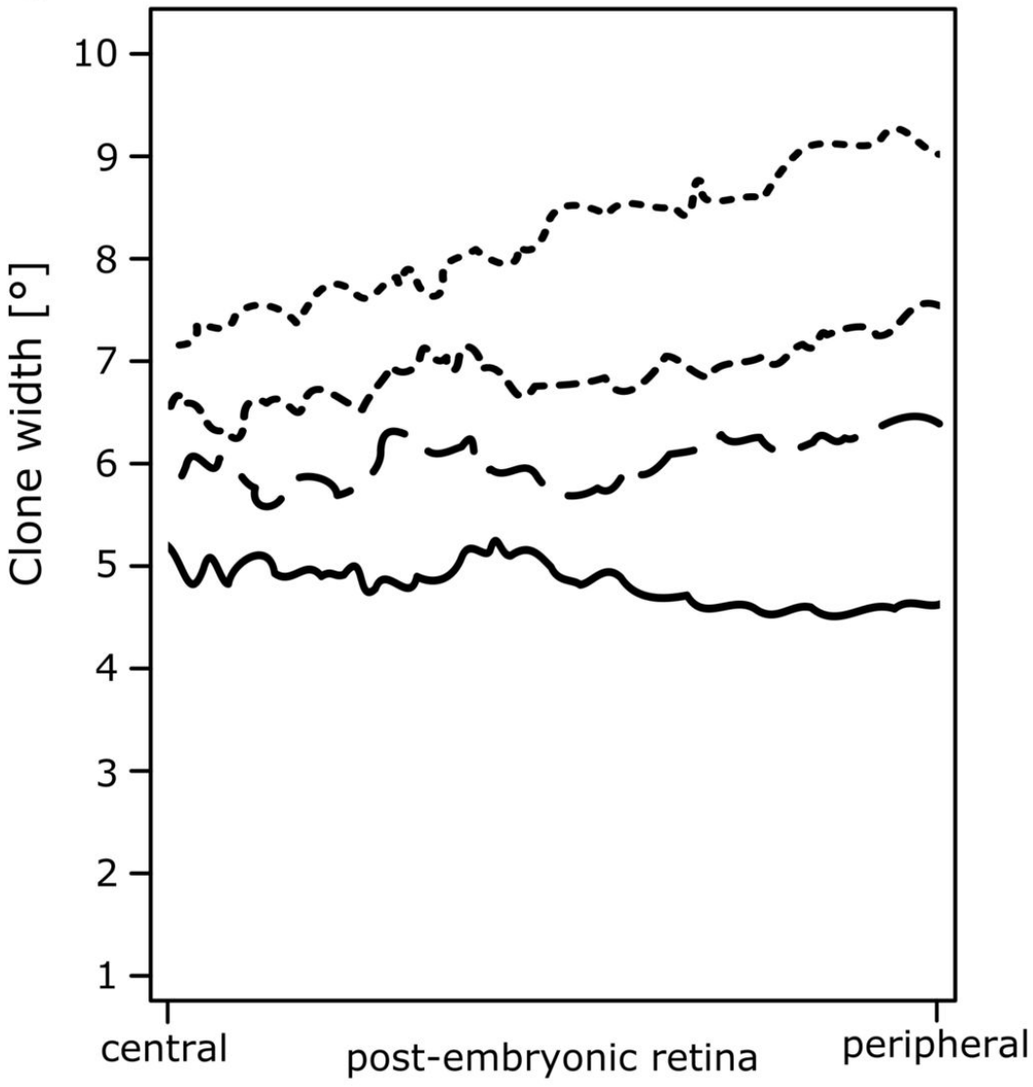

Simulation - p_{circ} = 0.000

Simulation - p_{circ} = 0.125

Simulation - p_{circ} = 0.250

Simulation - p_{circ} = 0.500

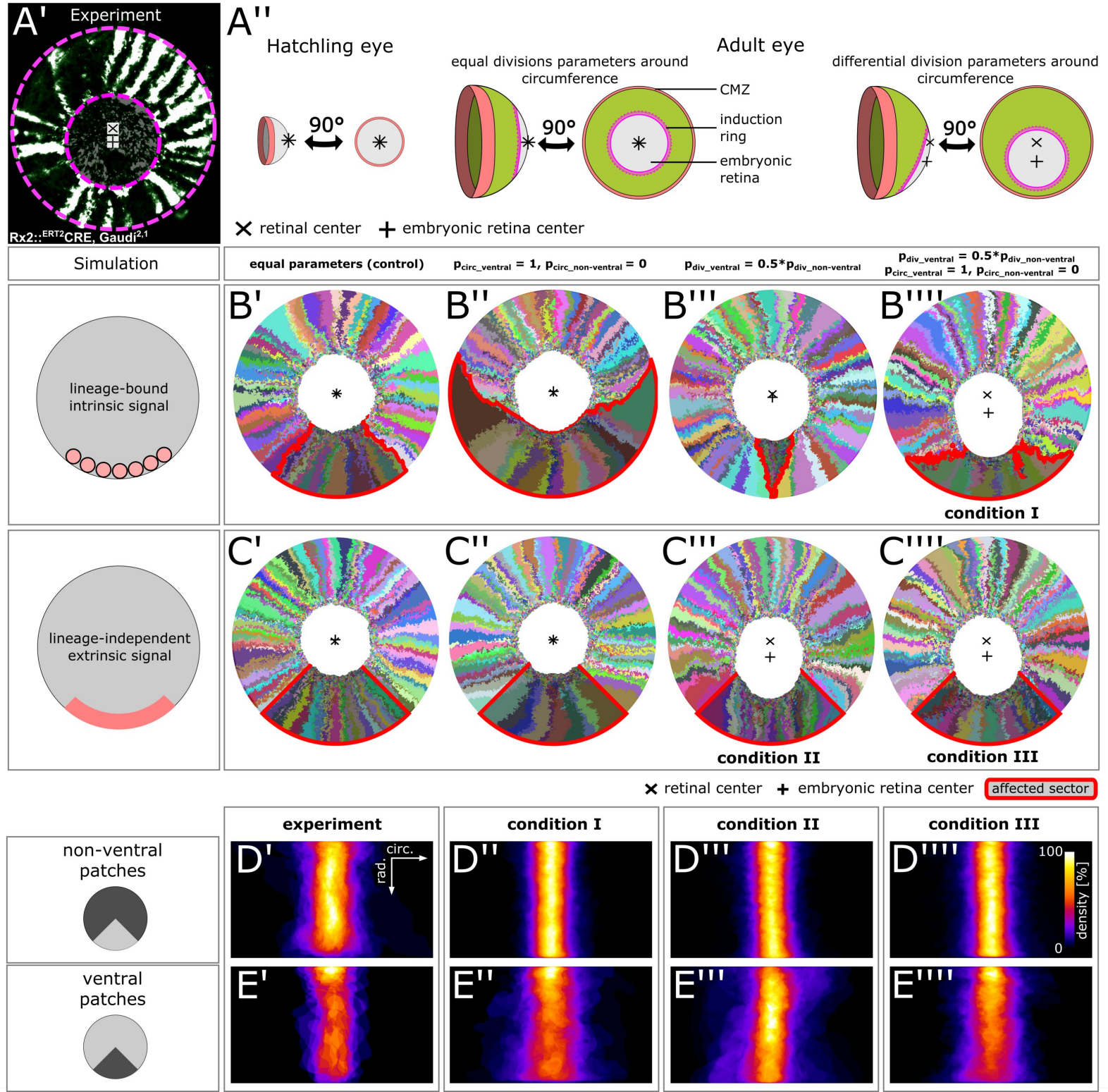
A'
Experiment
Rx2::ERT2CRE, Gaudi2,1
A''
Hatchling eye
90°
Adult eye
equal divisions parameters around circumference
CMZ
induction ring
embryonic retina
90°
differential division parameters around circumference
90°
× retinal center
+ embryonic retina center
Simulation
equal parameters (control)
p_circ_ventral = 1, p_circ_non-ventral = 0
p_div_ventral = 0.5*p_div_non-ventral
p_div_ventral = 0.5*p_div_non-ventral
p_circ_ventral = 1, p_circ_non-ventral = 0
lineage-bound intrinsic signal
B'
B''
B'''
B''''
condition I
lineage-independent extrinsic signal
C'
C''
C'''
C''''
condition II
condition III
× retinal center + embryonic retina center
affected sector
non-ventral patches
ventral patches
experiment
condition I
condition II
condition III
D'
circ.
rad.
D''
D'''
D''''
100
density [%]
0
E'
E''
E'''
E''''

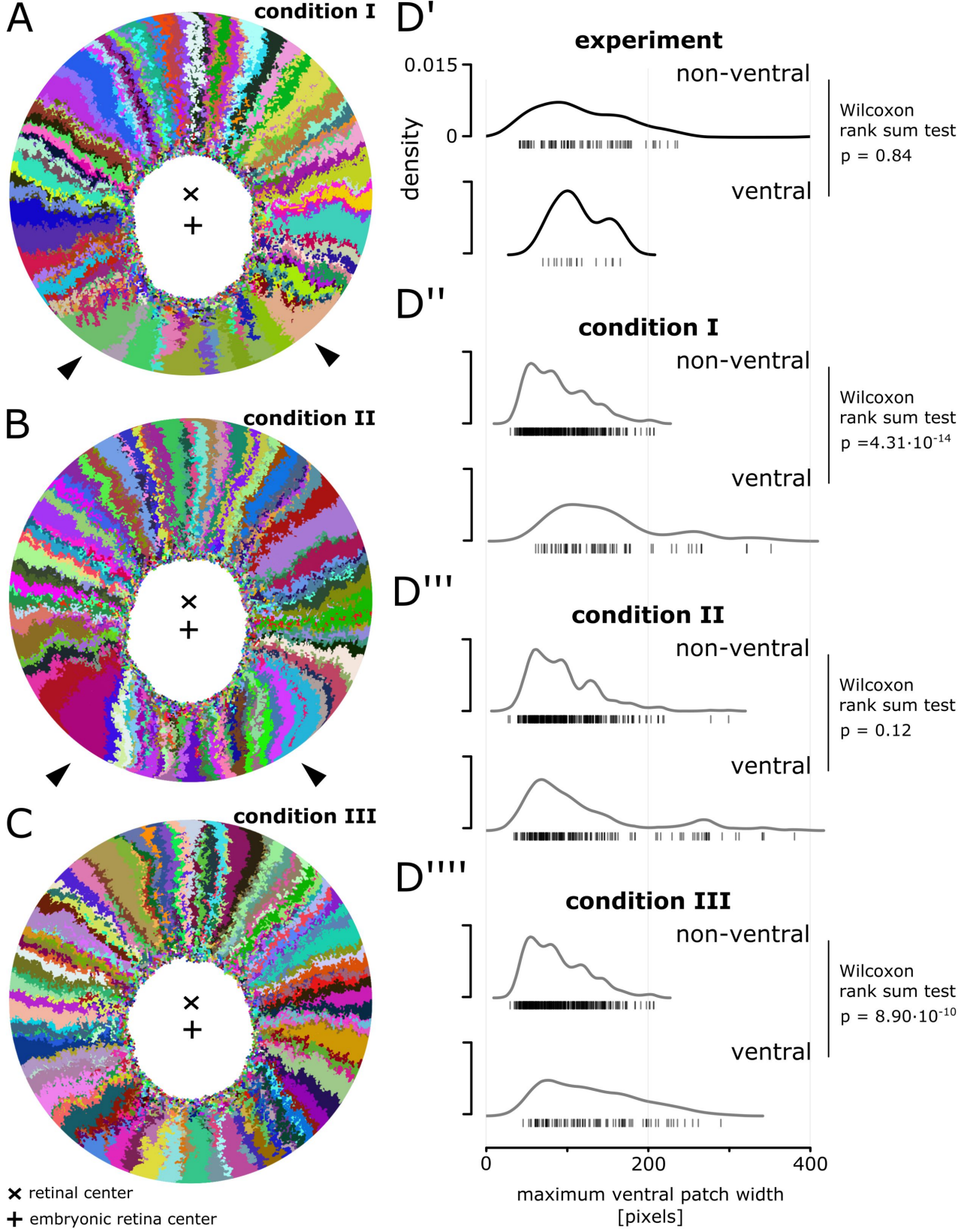
A
condition I
B
condition II
C
condition III
× retinal center
+ embryonic retina center
D'
experiment
0.015
0
density
non-ventral
ventral
Wilcoxon
rank sum test
p = 0.84
D''
condition I
non-ventral
ventral
Wilcoxon
rank sum test
p =4.31·10-14
D'''
condition II
non-ventral
ventral
Wilcoxon
rank sum test
p = 0.12
D''''
condition III
non-ventral
ventral
Wilcoxon
rank sum test
p = 8.90·10-10
0
200
400
maximum ventral patch width
[pixels]

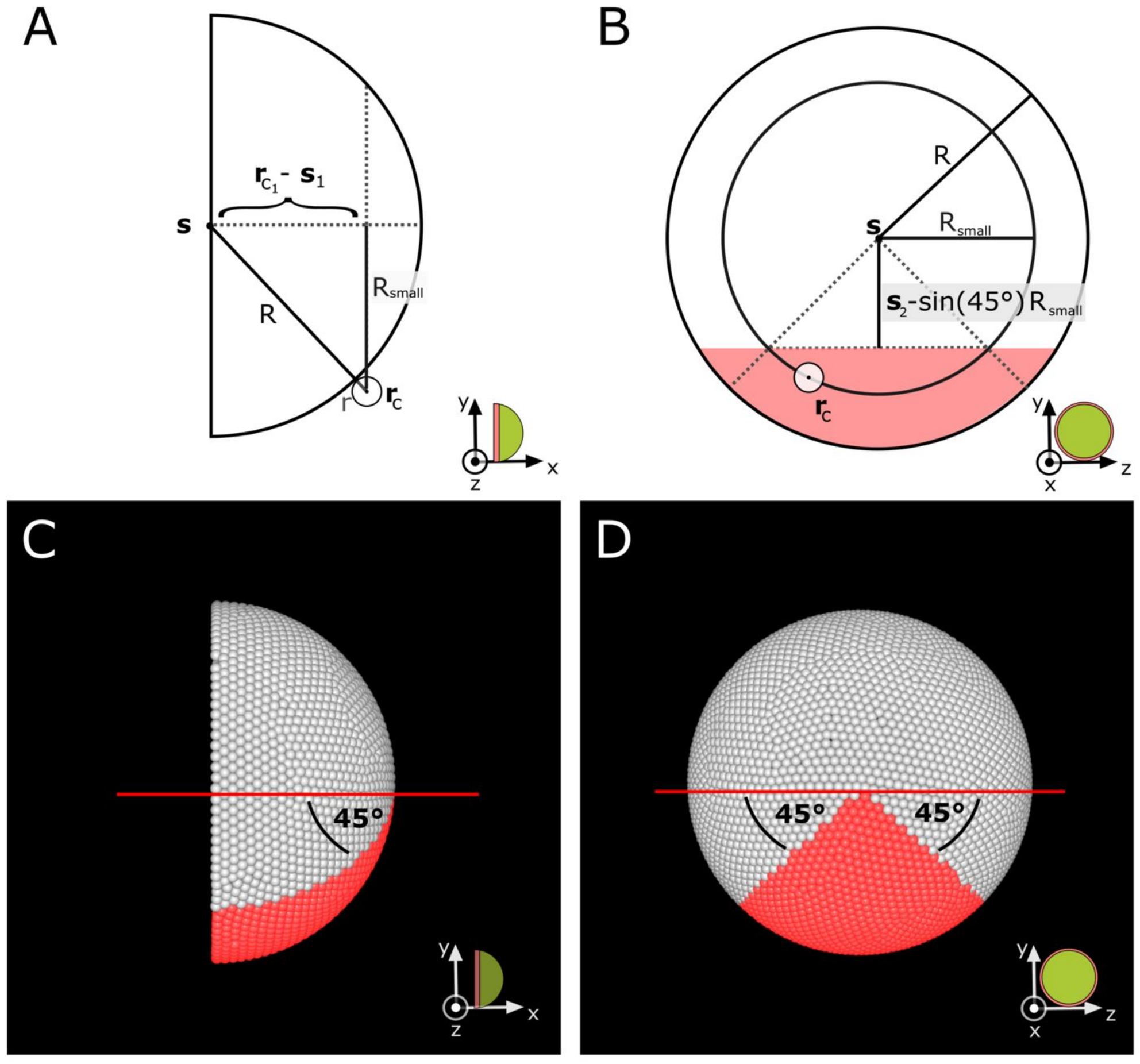
A
$\mathbf{r}_{C_1}$ - $\mathbf{s}_1$
s
R_{small}
R
$\mathbf{r}_C$
r
y
x
z
B
R
s
R_{small}
$\mathbf{s}_2$-sin(45°) R_{small}
$\mathbf{r}_C$
y
z
x
C
45°
y
x
z
D
45°
45°
y
z
x

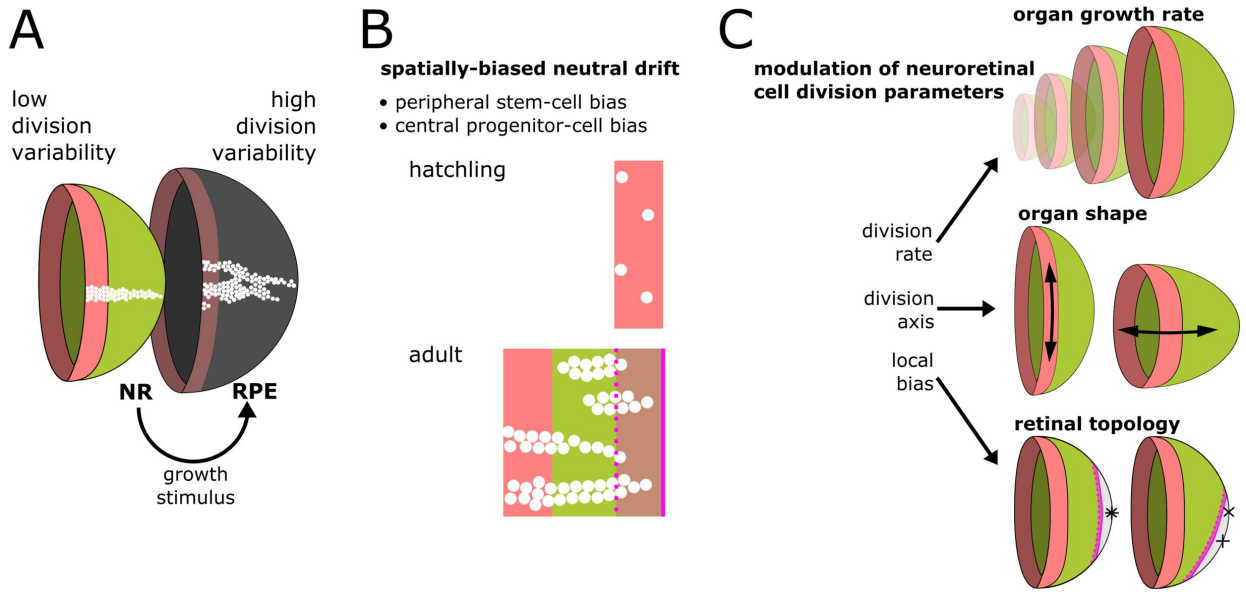
A
low
division
variability
high
division
variability
NR
RPE
growth
stimulus
B
spatially-biased neutral drift
• peripheral stem-cell bias
• central progenitor-cell bias
hatchling
adult
C
organ growth rate
modulation of neuroretinal
cell division parameters
division
rate
organ shape
division
axis
local
bias
retinal topology

Appendix 1

1. Center-based biomechanical model

The biomechanical model governing physical interactions between cells and all associated parameter values was adapted from previous work (Sütterlin *et al.*, 2017). The model is an off-lattice, center-based overlapping spheres model. Such cell center-based models allow cells to move freely in space and consider all forces as acting on a cell's center of mass. As previously described (Sütterlin *et al.*, 2017), cells in a simulation equilibrate the distance to each of their adjacent neighbors by exerting pressure or adhesion forces. Essentially, cells optimize the distance to all neighbors until they reach a target distance, which is a function of the cell's radius, the neighboring cells' radius, and the optimal cell-cell overlap (chosen by parameter scan to create a densely packed cell ensemble). In the absence of proliferation, cell death, and movement, all cells will reach a stable distance equilibrium. Additionally, the availability of space for the cells to move in (*e.g.* tissue boundaries) affects the distance equilibrium.

In the model extensions developed in this work, the distance equilibrium is continuously perturbed by proliferating cells in the CMZ, and cells are allowed to move only on the hemispherical surface area of the eye globe. In the following, we explain new model elements introduced in the current work.

2. Implementation of the fish eye model

2.1 Model initialization

We implement the eye globe as a sphere with an initial radius R_{init}, centered at $\mathbf{s}$, and constrain cells to remain on the surface of one hemisphere only. To generate the model's initial condition and achieve the initial distribution of cells on a hemisphere, we proceed in four steps.

1. Approximate the ideal number of cells N_{init} that fit on the initial hemispherical area based on the overlapping spheres model:

$$N_{init} = \left\lceil \frac{R_{\text{init}}^2}{\left(r\delta_{\text{ol}_{\text{max}}}\right)^2} \right\rceil, \quad (1)$$

where $\delta_{\text{ol}_{\text{max}}}$ is the optimal overlap between cells (Sütterlin *et al.*, 2017). Appendix 1 Eq. (1) is derived from the equation for the curved surface area of a hemisphere and the assumption that each cell occupies a circular area proportional to its radius and the optimal overlap.

2. Obtain a set of nodes by subdividing an icosahedral mesh on the sphere.
3. Place a cell c on a mesh node located at $\mathbf{r}_c$ if it satisfies the condition

$$\mathbf{r}_{c_1} > \mathbf{s}_1 , \tag{2}$$

where the subscript *1* denotes the x-component of the 3-dimensional vectors. This condition ensures that only one hemisphere is populated by cells. Step 3 is repeated until all N_{init} cells have been placed.

4. Simulate biomechanical forces using the model developed in (Sütterlin *et al.*, 2017) until cells reach equilibrium, which is defined by the average displacement of all cells falling under a threshold μ

$$\sum_{i=1}^{N_{\text{init}}} \frac{d\mathbf{r}}{dt} < \mu . \tag{3}$$

2.2 Constraining cells to the hemisphere's surface

Since the eye grows slowly over a period of several months, the growth process can be considered quasi-static. The tissues we model in this work consist of hemispherically arranged cell ensembles without mixing of cells along the direction normal to their hemispherical layer. In the center-based overlapping spheres model, the balance of forces can result in cell displacement in any direction. To restrict movement along the normal direction, we reposition cells at the end of each biomechanical force calculation step Δt (Figure 2 Supplement 2). The force balance is then iteratively recalculated with the new cell position, allowing the cell ensemble in the simulation to reach a distance equilibrium on the curved hemispherical surface. In total, each simulation step consists of 100 such iterations.

For a cell c at $\mathbf{r}_c$, we obtain the new location $\tilde{\mathbf{r}}_c$ by rescaling the unit vector from the hemisphere's center $\mathbf{s}$ to $\mathbf{r}_c$ with the eye radius at a given simulation step $R(t)$

$$\tilde{\mathbf{r}}_c = \frac{\mathbf{s} - \mathbf{r}_c}{\left\| \mathbf{s} - \mathbf{r}_c \right\|} R(t) . \tag{4}$$

To constrain cells to one hemisphere only, we introduce a ring of tightly packed immobile "obstacle cells" on the sphere's equator that produce a biomechanical roadblock and do not otherwise participate in the simulation (Figure 2 Supplement 3). Force balance between cells in the simulation and obstacle cells is calculated without using the adhesive term (Sütterlin *et al.*, 2017).

2.3 Growth of the eye globe

Growth of the eye globe is achieved by increasing its radius R; the eye globe is strictly spherical in all simulations. Computationally, inducer and responder growth mode differ in the calculation of the radius R.

We define the inducer growth mode as growth of the eye globe controlled by the cells in the tissue under consideration. For the computational implementation, we assume that every time a cell divides, the eye surface area increases such that the new total number of cells can achieve its target distance equilibrium without any limitation from the available space. In other words, the eye globe grows just enough to generate the surface area required for housing all cells. Thus, we use the following growth equation in simulations of the inducer growth mode:

$$R(t) = \sqrt{\frac{N_{\text{cells}}(t)\left(r\delta_{\text{ol}_{\max}}\right)^2}{2}}\,, \tag{5}$$

where $N_{\text{cells}}(t)$ is the total number of cells at simulation step t that emerges from the simulation. This equation is constructed analogously to Appendix 1 Eq. (1), and here too we take into consideration the optimal overlap between cells $\delta_{\text{ol}_{\max}}$. Since in our model there is no cell death, $N_{\text{cells}}(t)$ never decreases, and likewise the radius R never decreases.

We define the responder growth mode as growth of the eye globe independent from the cells in the tissue under consideration. Thus, we formulate the growth equation:

$$R(t) = R_{\text{init}} + c_{\text{R}}t\,, \tag{6}$$

and set c_{R} as a constant. In short, the radius of the eye globe grows at a constant linear rate in all simulations with the responder growth mode.

2.4 Cell division

The flowchart in Figure 2 Supplement 1 summarizes the decisions that govern cell proliferation that will be described in the following paragraphs.

Proliferative cells commit to cell division with a probability p_{division} at every simulation step. If the minimum cell cycle time $t_{\text{cellCycle}}$ has not been attained the division is delayed until this time elapsed, otherwise cells divide immediately. As in other cell-center agent based models, we introduce a rule that forbids cell division if the local cell density is too high (Pathmanathan *et al.*, 2009; Osborne *et al.*, 2017; Sütterlin *et al.*, 2017). We implement this rule as follows: We calculate local cell packing for a cell c as the average overlap to all neighboring cells n_i

; cell division is not permitted if the average overlap exceeds a threshold proportional to the cell diameter

$$\frac{\sum_{i=1}^{n} d_{ol}\left(\mathbf{r}_c, \mathbf{r}_{n_i}\right)}{n} > 2r\delta_{\text{ol\_threshold}}\,, \tag{7}$$

where $d_{ol}\left(\mathbf{r}_c, \mathbf{r}_{n_i}\right)$ is the overlap between cell c and neighboring cell n_i that emerges from the simulation, and $\delta_{\text{ol\_threshold}}$ is a model parameter.

Together with the function for the growth of the eye globe (section 2.3), the value for the overlap threshold $\delta_{\text{ol\_threshold}}$ determines the main difference between inducer and responder growth modes. A small value means that a smaller average overlap is sufficient to arrest the cell cycle (cells arrest at lower densities).

For considerations on the parameter values for $\delta_{\text{ol\_threshold}}$ see section 3.2.

2.5 Positioning of daughter cells after division

The introduction of new cells into the simulation follows the general procedure used in cell-center agent-based models as previously described (Sütterlin *et al.*, 2017). Briefly, when a cell j located at $\mathbf{r}_j = \begin{pmatrix} x_j & y_j & z_j \end{pmatrix}^{\mathbf{T}}$ divides, a new cell k is introduced into the simulation at position $\mathbf{r}_k = \begin{pmatrix} x_k & y_k & z_k \end{pmatrix}^{\mathbf{T}}$. The initial distance between cells $\left|\mathbf{r}_k - \mathbf{r}_j\right|$ is chosen to be a small non-zero value. The coordinates $\mathbf{r}_j$ and $\mathbf{r}_k$ are fed as initial input to the biomechanical model, which then calculates how force balance repositions the cells. This means that initially, the two daughter cells almost completely overlap and then gradually separate, displacing any neighboring cells in a “domino effect“. Thus, the final position of the daughter cells at the beginning of the simulation step following division may not fully correspond to the initial position that is calculated upon division, but is biased by it.

In this work, we introduce modifications in the calculation of $\mathbf{r}_k$ to allow cells to divide along a given pre-determined direction, which we explain in the following.

By default, cells divide with random division axis, where we calculate $\mathbf{r}_k$ as

$$\mathbf{r}_k = \begin{pmatrix} x_j \\ y_j \\ z_j \end{pmatrix} + \rho \begin{pmatrix} X - 0.5 \\ X - 0.5 \\ X - 0.5 \end{pmatrix}, \tag{8}$$

where X is a uniformly distributed random number in the interval $[0,1]$, and ρ is a scaling constant that defines the maximum initial distance between daughter cells.

In simulations with directed division axes, we use different calculations for radial and circumferential divisions. When cell j divides radially, we calculate $\mathbf{r}_k$ as

$$\mathbf{r}_k = \begin{pmatrix} x_j \\ y_j \\ z_j \end{pmatrix} + Y \frac{\rho}{2} \begin{pmatrix} 1 \\ 0 \\ 0 \end{pmatrix}, \tag{9}$$

where Y is a number chosen uniformly at random from the set $(-1,1)$. When cell j divides circumferentially, we calculate $\mathbf{r}_k$ as

$$\mathbf{r}_k = \begin{pmatrix} x_j \\ y_j \\ z_j \end{pmatrix} + Y \frac{\rho}{2} \begin{pmatrix} 0 \\ 1 \\ 1 \end{pmatrix}. \tag{10}$$

The probability for a cell j to choose a radial or circumferential division axis depends on probabilities based on geometry derived in the following.

A hemispherical eye of radius R has an area of

$$A_{\text{eye}} = 2\pi R^2. \tag{11}$$

The CMZ forms a band of width w at the base of the eye, and has an area of

$$A_{\text{CMZ}} = 2\pi R w. \tag{12}$$

Thus, the area ratio between the eye without the CMZ and the CMZ is

$$\frac{A_{\text{eye}} - A_{\text{CMZ}}}{A_{\text{CMZ}}} = \frac{R - w}{w} = \frac{R}{w} - 1. \tag{13}$$

To obtain $\frac{R}{w} - 1$ radial divisions for every circumferential division, we formulate the probability of a radial division as

$$p_{\text{rad}} = \frac{\frac{R}{w} - 1}{\frac{R}{w} - 1 + 1} = 1 - \frac{w}{R}, \tag{14}$$

and the probability for circumferential divisions as

$$p_{\text{circ}} = 1 - p_{\text{rad}} = \frac{w}{R}. \tag{15}$$

2.6 Simulations with differential divisions in the ventral sector

We define the ventral sector as a 90° sector on the hemisphere (Figure 6 Supplement 2). To determine if a given cell c located at $\mathbf{r}_c$ lies in this sector, we first calculate the radius of a small circle on the hemisphere enlarged by the radius of the cell c:

$$R_{\text{small}}(t) = \sqrt{\left(R(t) + r\right)^2 - \left(\mathbf{r}_{c_1} - \mathbf{s}_1\right)^2}, \tag{16}$$

where r is the cell radius, R is the radius of the hemisphere, and $\mathbf{r}_{c_1}$ and $\mathbf{s}_1$ denote the x-component of $\mathbf{r}_c$ (cell position) and $\mathbf{s}$ (center of eye globe), respectively. A cell lies in the ventral sector if the following holds:

$$\mathbf{r}_{c_2} < \mathbf{s}_2 - \sin(45°) R_{\text{small}}(t), \tag{17}$$

$\mathbf{r}_{c_2}$ and $\mathbf{s}_2$ denote the y-component of $\mathbf{r}_c$ and $\mathbf{s}$, respectively.

In simulations with a lineage-independent extrinsic signal, cells in the non-ventral and ventral sectors are redefined at every simulation step according to Appendix 1 Eqs. (16-17). Cells in the non-ventral sector choose their division axis according to Appendix 1 Eq. (9), while cells in the ventral sector with a circumferential division axis bias use Appendix 1 Eq. (10) (defaulting to Appendix 1 Eq. (9) in simulations without the circumferential division axis bias).

In simulations with a lineage-bound intrinsic signal, Appendix 1 Eqs. (16-17) are used in simulation step 0 to define which lineages belong to the ventral and non-ventral sectors. All progeny of non-ventral lineages choose their division axis according to Appendix 1 Eq. (9). The division axis of progeny of ventral lineages defaults to Appendix 1 Eq. (9) unless they have a circumferential division axis bias, in which case they follow Appendix 1 Eq. (10).

2.7 Cell differentiation

We implement two cell types in the virtual eye: differentiated cells and proliferative (stem) cells. All divisions produce identical proliferative daughter cells. The fate of cells depends on their position on the virtual eye hemisphere. A cell c at $\mathbf{r}_c$ becomes a differentiated cell type if it moves beyond the width of the CMZ:

$$\mathbf{r}_{c_1} > \mathbf{s}_1 + w, \tag{18}$$

where $\mathbf{r}_{c_1}$ and $\mathbf{s}_1$ denote the x-component of $\mathbf{r}_c$ (cell position) and $\mathbf{s}$ (center of eye globe), respectively. Differentiated cells cannot revert to proliferative cells.

3. Model parameters

Parameter values used in the simulations presented in this work are listed in Appendix 1 Table 1. Unless otherwise stated, we used the same parameter values for all simulations.

In the following sections, we discuss the rationale for choosing parameter values that are not fixed by experimental observations.

3.1 Minimal displacement threshold

To ensure that cells are well-distributed on the hemispherical surface for the initial condition of the simulation, we place a predetermined number of cells on the surface and simulate the biomechanical model until cell displacement minimizes (see section 2.1). Numerical fluctuations lead to a small baseline cell displacement, therefore requiring a threshold cut-off value, which we call μ. In the absence of such a threshold, the simulation converges to a value of $0.07\mu m$ average cell displacement (1/100 of a cell's diameter; Appendix 1 Figure 1 E). Values of μ between $0.07\mu m$ – $0.2\mu m$ result in similar arrangements of evenly-distributed cells (Appendix 1 Figure 1 A-B). At $\mu = 0.7\mu m$ cells failed to completely cover the hemisphere, leaving a small gap (Appendix 1 Figure 1 C). At $\mu = 20\mu m$ there is no biomechanical calculation and cells were unequally distributed with local dense foci and large empty spaces (Appendix 1 Figure 1 D). To minimize the calculation time while still obtaining an even cell distribution, we chose $\mu = 0.2\mu m$.

3.2 Overlap threshold

In the complete absence of coupling between cell division and eye growth, the growth rate may exceed cell production rate, resulting in few cells dispersed over a large surface (Appendix 1 Figure 2 A'-A''''). In the opposite case where cell production exceeds organ growth rate, cells become packed to a physically implausible degree (Appendix 1 Figure 2 B'-B''''). As cell density and thus inter-cell forces increase, some cells escape through the layer of obstacle cells and proliferate on the unused half of the sphere (Appendix 1 Figure 2 B'' inset, B'''-B'''').

To couple eye growth to cell proliferation, we introduce an overlap threshold $\delta_{\text{ol\_threshold}}$ (see sections 2.3 and 2.4). Cells in the inducer growth mode are, by definition, less sensitive to density-dependent arrest, while cells in the responder growth mode are more sensitive. This

means that the overlap threshold in the inducer growth mode should exceed the overlap threshold in the responder growth mode: $\delta_{\text{ol\_threshold\_inducer}} > \delta_{\text{ol\_threshold\_responder}}$. We performed a parameter scan (Appendix 1 Figure 2 D'-G'') to determine values for $\delta_{\text{ol\_threshold}}$ such that:

I) In the inducer growth mode, density-dependent cell cycle arrest is minimal.

II) In the responder growth mode, density-dependent cell cycle arrest is maximal **and** cells are not completely arrested.

In the inducer growth mode, growth of the radius depends on the total number of cells in the simulation (Appendix 1 Eq. (5)). Thus, growth rate increases as the overlap threshold is increased (Appendix 1 Figure 2 G'). A value of $\delta_{\text{ol\_threshold}} = 0.1$ completely inhibits cell proliferation, as the equilibrium average overlap normalized to the cell diameter (normalized average overlap) exceeds the threshold value (Appendix 1 Figure 2 D'). As a result, the organ does not grow at all (Appendix 1 Figure 2 G', solid black line). At $\delta_{\text{ol\_threshold}} = 0.2$, a large population of cells in the proliferative domain (located at the periphery of the radius; indicated by solid pink bar) exceeds the threshold (Appendix 1 Figure 2 D''). Generation of new cells through division increases the local cell density, resulting in inhibition of proliferation due to the low overlap threshold and a gradual reduction in growth rate (Appendix 1 Figure 2 G' orange dashed line). At $\delta_{\text{ol\_threshold}} = 0.3$, only few cells exceed the threshold (Appendix 1 Figure 2 D'''), and growth is almost unconstrained (Appendix 1 Figure 2 G' green dashed line). At $\delta_{\text{ol\_threshold}} = 0.4$, no cells exceed the threshold and growth is completely unconstrained (Appendix 1 Figure 2 G' cyan dashed line). Thus, this condition fulfills requirement I. At all values of $\delta_{\text{ol\_threshold}}$, the ratio between total area required by cells and the hemisphere area (area ratio) is equal to 1 throughout the simulation, meaning that - on average - cells are evenly distributed and ideally packed (Appendix 1 Figure 2 F').

In the responder growth mode, the radius of the hemisphere steadily grows regardless of the number of cells in the simulation (Appendix 1 Figure 2 G''). A value of $\delta_{\text{ol\_threshold}} = 0.1$ strongly inhibits cell proliferation, but as the radius grows cells become dispersed and eventually go under the threshold allowing some proliferation (Appendix 1 Figure 2 E'). However, the area ratio of cells to hemisphere steadily decreases indicating the formation of inter-cell gaps (Appendix 1 Figure 2 F'' solid black line). At $\delta_{\text{ol\_threshold}} = 0.2$, many, but not all, cells are inhibited (Appendix 1 Figure 2 E''), and the area ratio is near 1 throughout the simulation (Appendix 1 Figure 2 F'' orange dashed line). At $\delta_{\text{ol\_threshold}} = 0.3$ and $\delta_{\text{ol\_threshold}} = 0.4$, cell proliferation overtakes area growth, resulting in high cell packing all

over the hemisphere (Appendix 1 Figure 2 E''' and E''''). As a result, the area ratio increases over time (Appendix 1 Figure 2 F'' green and cyan dashed lines), until cell packing becomes so severe that cells escape through the obstacle cell layer and proliferate exponentially on the unused half of the sphere (Appendix 1 Figure 2 F'' pink asterisk). Given these data, a value of $\delta_{\text{ol\_threshold}} = 0.2$ best fulfills requirement II while generating an even distribution of cells on the hemisphere for the full duration of the simulation.

3.3 Proliferation probability, minimum cell cycle, and growth rate of the retinal radius

A hatchling medaka grows to sexual maturity within 2 - 3 months. Growth rates vary between individuals, and retinae recovered from young adult fish have radii in the range of 600 - 800 µm. During this period, if fish are regularly fed and reared at low individual density, growth is approximately linear (Appendix 1 Figure 3 A), so the growth rate of the retinal radius can be estimated to range from

$$\frac{600[\mu\text{m}]\text{-}100[\mu\text{m}]}{90 \cdot 24[\text{h}]} \approx 0.23 \frac{\mu\text{m}}{\text{h}} \tag{19}$$

to

$$\frac{800[\mu\text{m}]\text{-}100[\mu\text{m}]}{60 \cdot 24[\text{h}]} \approx 0.49 \frac{\mu\text{m}}{\text{h}}. \tag{20}$$

Cell division intervals are not characterized in post-embryonic retinal stem cells. In other proliferative stem cell systems, such as mouse tail skin, cell division intervals follow a right-skewed distribution, which can be modeled by combining a minimum division interval with a fixed probability for division (Klein *et al.*, 2007). In the absence of a minimum cell cycle, division intervals in this model follow an exponential distribution, and would thus allow manifestly unphysiological cell cycle times that can be arbitrarily short (Klein *et al.*, 2007).

Our cell proliferation model assumes that a cell may commit to cell division at any time with probability p_{div}, but must wait a minimum of $t_{\text{cellCycle}}$ simulation steps before actually dividing. These rules generate a distribution of cell cycle intervals with a peak at $t_{\text{cellCycle}}$ and exponential decrease thereafter (Appendix 1 Figure 3 B-C). The magnitude of the peak and the exponential decay increase with increasing p_{div} (Appendix 1 Figure 3 B). As expected, increasing $t_{\text{cellCycle}}$ shifts the distribution to the right, and also increases the peak (Appendix 1 Figure 3 C).

By parameter scan, we determined which combinations of p_{div} and $t_{\mathrm{cellCycle}}$ result in growth rates within the range in Appendix 1 Eqs. (19-20) (Appendix 1 Figure 3 D). Different values for p_{div} and $t_{\mathrm{cellCycle}}$ in inducer and responder growth mode resulted in qualitatively similar clone properties (Appendix 1 Figure 3 E'-E'''' (inducer), F'-F'''' (responder)). The parameters we chose for the simulations presented in the manuscript fall in the middle of this biologically plausible range (white star in Appendix 1 Figure 3 D).

Appendix 1 Figure 1. A minimum displacement threshold μ = 0.2 ensures even cell distribution
Different views of initial condition of the simulation with (**A**) μ = 0.07 μm, (**B**) μ = 0.2 μm, (**C**) μ = 0.7 μm, (**D**) μ = 20.0 μm. (**E**) Calculation time plotted against the average cell displacement during initialization of the simulation. The simulation converges to 0.07 μm average displacement threshold (pink dashed line).

Appendix 1 Figure 2. Parameter scan to determine optimal overlap threshold values.
(**A'-B''''**) Different views of representative simulations lacking coupling between eye radius growth and cell proliferation. (**A'-A''**) Eye area growth rate exceeds cell proliferation rate, resulting in cell dispersion. (**A'''-A''''**) Magnification of inset in (A'') showing peripheral cells without (A''') or with (A'''') obstacle cells displayed. (**B'-B''**) Cell proliferation rate exceeds eye area growth rate, resulting in extremely dense cell packing. (**B'''-B''''**) Magnification of inset in (B'') showing peripheral cells without (B''') or with (B'''') obstacle cells displayed. Three cells have squeezed through the obstacle cell layer. (**D'-E''''**) Normalized average overlap of cells at simulation step 1400 plotted against their position along the normalized radius. Dashed pink line: Value of $\delta_{\text{ol\_threshold}}$ used for the respective simulation. Solid pink bar: Extent of virtual CMZ. (D-D'''') inducer growth mode; (E'-E'''') responder growth mode. (**F'-F''**) Ratio between total area required by cells and total eye area from simulation step 0 to simulation step 1400 for different values of $\delta_{\text{ol\_threshold}}$. (F') inducer growth mode; (F'') responder growth mode. Pink asterisk marks approximate time when cells start squeezing through obstacle cell layer. (**G'-G''**) Growth of the eye radius from simulation step 0 to simulation step 1400 for different values of $\delta_{\text{ol\_threshold}}$. (G') inducer growth mode; (G'') responder growth mode.

Appendix 1 Figure 3. Parameter scan of minimum cell cycle and division probability.
(**A**) Experimental data. Both body length (green) and eye diameter (magenta) grow approximately linearly over the first 90 days after hatching. (**B**) Distribution of cell division intervals with fixed $t_{\text{cellCycle}}$ and variable p_{div}. (**C**) Distribution of cell division intervals with variable $t_{\text{cellCycle}}$ and fixed p_{div}. (**D**) Eye growth rates in the simulation determined from a parameter scan of $t_{\text{cellCycle}}$ and p_{div} entailing over 150 simulation runs; intermediate values were interpolated. The plausible parameter space estimated from experimental measurements is contoured by black lines. Open white circles represent values for simulations depicted in (B, C, E'-E'''', F'-F''''). White star represents values used for simulations in the main manuscript. (**E'-E''''**) Representative simulations of the inducer growth mode at different values for $t_{\text{cellCycle}}$ and p_{div}. (**F'-F''''**) Representative simulations of the responder growth mode at different values for $t_{\text{cellCycle}}$ and p_{div}.

290 **Appendix 1 Table 1 Model parameters.** Parameters for the force balance calculation of the
291 biomechanical model are identical to previous work (Sütterlin *et al.*, 2017) and are not listed.

Description	Parameter	Value	Reference/Explanation
Biomechanical model parameters			
Biomechanical calculation step.	Δt	36 s	(Sütterlin *et al.*, 2017)
Seconds per simulation step.	t_{simstep}	3600 s [simstep]$^{-1}$	(Sütterlin *et al.*, 2017)
Optimal overlap for obstacle cells.	$\delta_{\mathrm{ol}_{\mathrm{obstacleCells}}}$	0.5	Determined by parameter scan to create a tight barrier to cell movement.
Optimal overlap for retinal cells.	$\delta_{\mathrm{ol}_{\mathrm{max}}}$	0.85	(Sütterlin *et al.*, 2017)
Initial distance between daughter cells.	ρ	0.005 µm	(Sütterlin *et al.*, 2017)
Initial condition parameters			
Initial radius of eye globe.	R_{init}	100 µm	Estimated from preparations of hatchling eyes.
Minimal displacement threshold.	μ	0.2 µm	Determined by parameter scan to generate even initial cell distribution.
Simulation parameters			
Retinal cell radius.	r	3.5 µm	Estimated from histological sections.
Width of the stem cell domain.	w	25 µm	Estimated from histological sections.
Overlap threshold beyond which cell cycle is arrested.	$\delta_{\mathrm{ol\_threshold}}$	0.4	*Value for inducer growth mode.* Estimated from parameter scan to minimize density-dependent cell cycle arrest.
		0.2	*Value for responder growth mode.* Estimated from parameter scan to maximize density-dependent cell cycle arrest without completely suppressing division.
Minimal cell cycle length.	$t_{\mathrm{cellCycle}}$	24 h	Chosen to produce a plausible biological growth rate.
Probability of cell division.	p_{division}	$\frac{1}{26}$ h^{-1}	Chosen to produce a plausible biological growth rate.
		$\frac{1}{52}$ h^{-1}	*Value for ventral lineages with differential behavior.*
Growth rate of the eye radius (*only in responder growth mode*).	c_{R}	$6.94 \cdot 10^{-5}$ µm s^{-1}	Chosen as a small value to ensure quasi-static growth within the biologically plausible growth rate range.

292

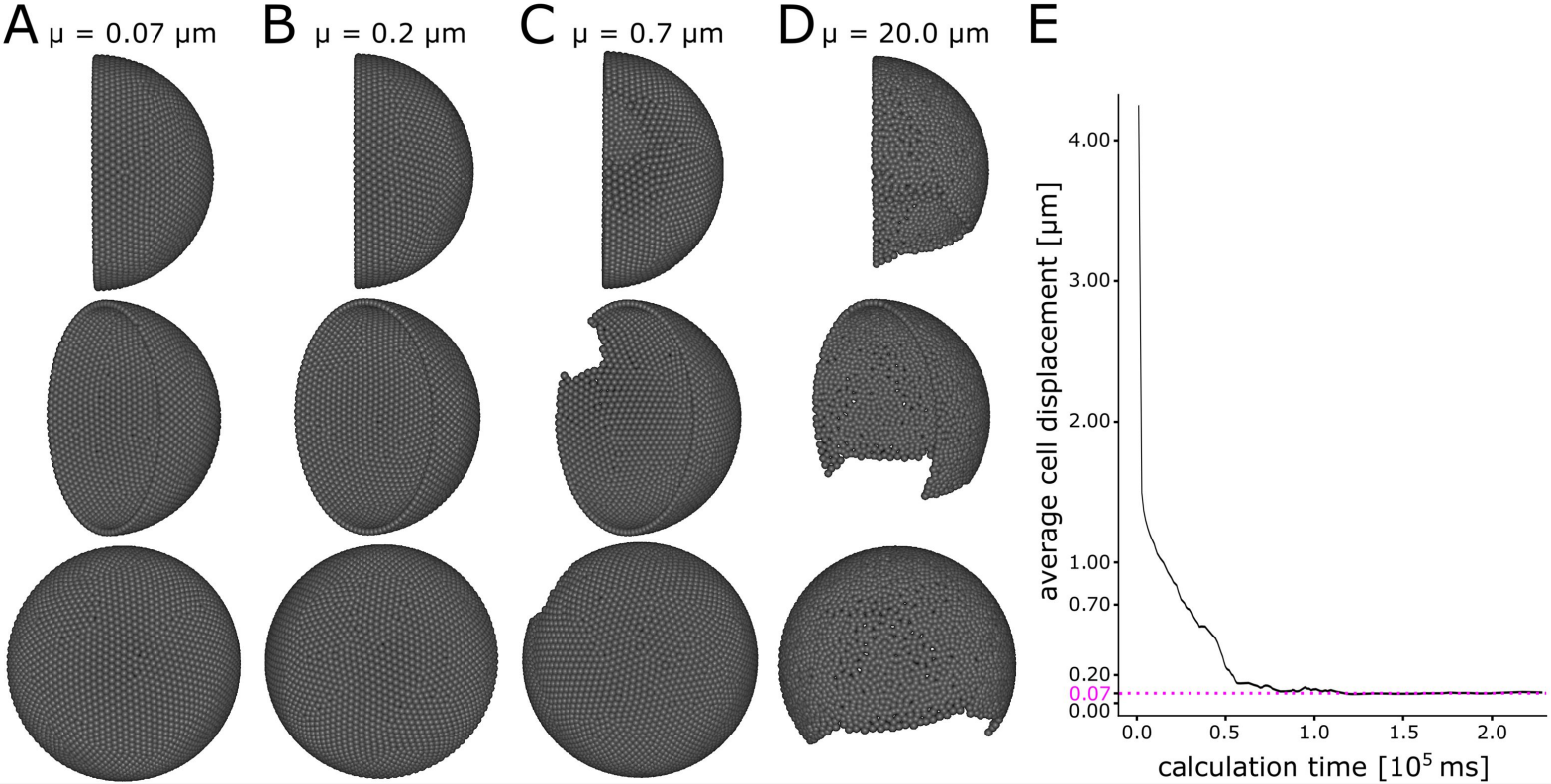
A μ = 0.07 μm
B μ = 0.2 μm
C μ = 0.7 μm
D μ = 20.0 μm
E
average cell displacement [μm]
4.00
3.00
2.00
1.00
0.70
0.20
0.07
0.00
0.0
0.5
1.0
1.5
2.0
calculation time [10^5 ms]

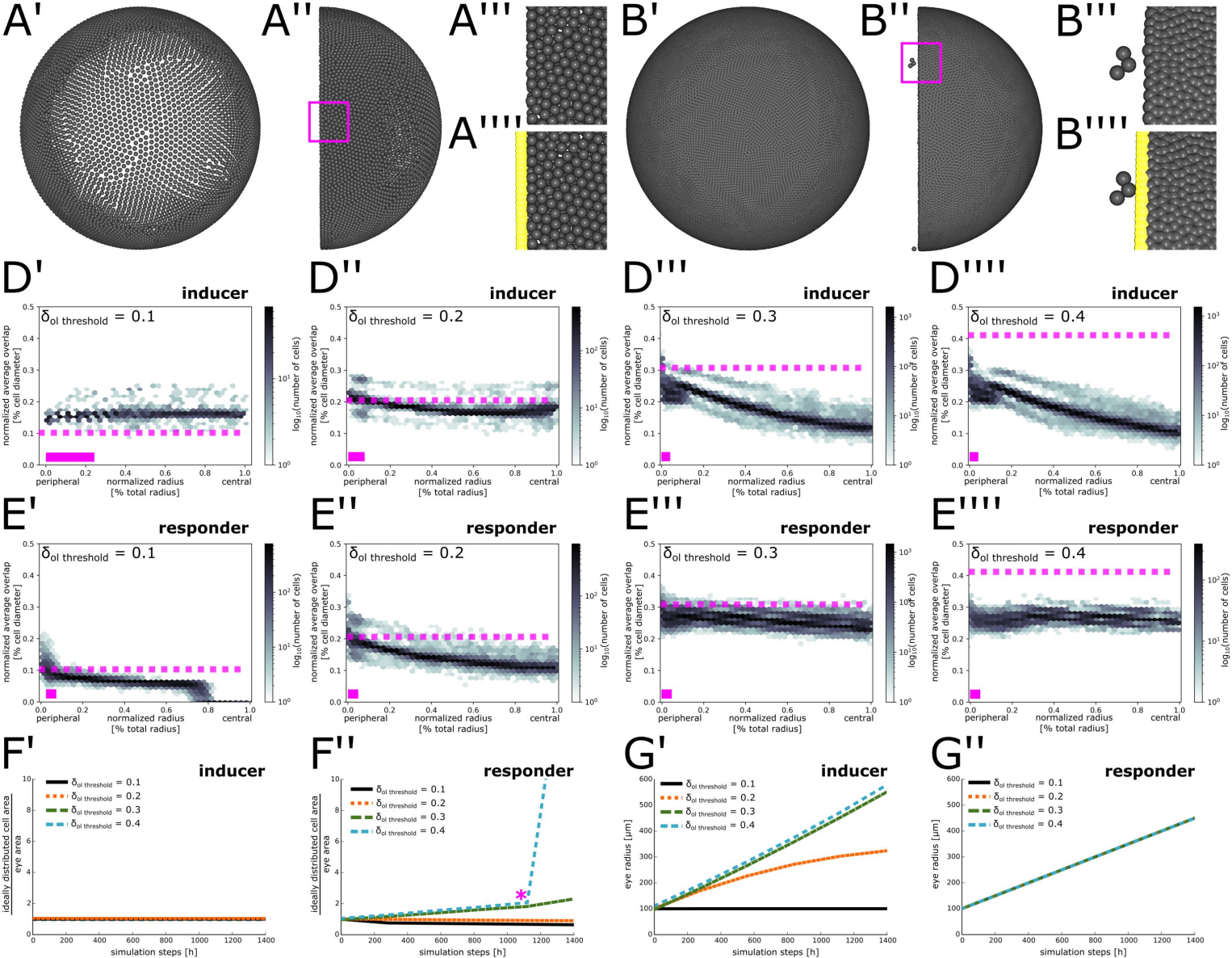
A'
A''
A'''
A''''
B'
B''
B'''
B''''
D'
inducer
δol threshold = 0.1
D''
inducer
δol threshold = 0.2
D'''
inducer
δol threshold = 0.3
D''''
inducer
δol threshold = 0.4
normalized average overlap [% cell diameter]
log10(number of cells)
peripheral
normalized radius [% total radius]
central
E'
responder
δol threshold = 0.1
E''
responder
δol threshold = 0.2
E'''
responder
δol threshold = 0.3
E''''
responder
δol threshold = 0.4
F'
inducer
F''
responder
ideally distributed cell area / eye area
δol threshold = 0.1
δol threshold = 0.2
δol threshold = 0.3
δol threshold = 0.4
simulation steps [h]
G'
inducer
G''
responder
eye radius [µm]
simulation steps [h]

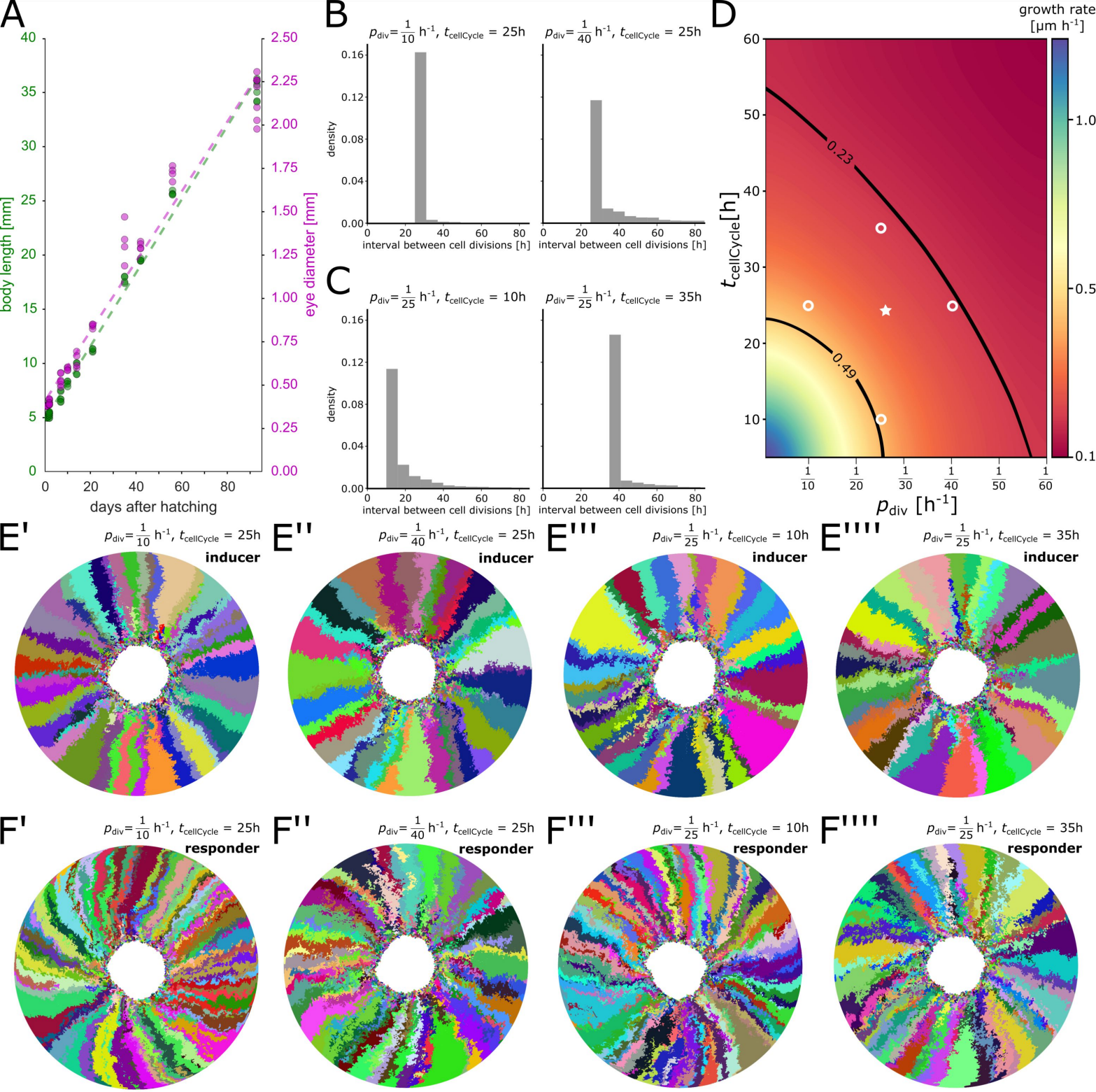
A
body length [mm]
eye diameter [mm]
days after hatching
B
$p_{div}=\frac{1}{10}$ h^{-1}, $t_{cellCycle}$ = 25h
$p_{div}=\frac{1}{40}$ h^{-1}, $t_{cellCycle}$ = 25h
density
interval between cell divisions [h]
C
$p_{div}=\frac{1}{25}$ h^{-1}, $t_{cellCycle}$ = 10h
$p_{div}=\frac{1}{25}$ h^{-1}, $t_{cellCycle}$ = 35h
D
growth rate [µm h^{-1}]
0.23
0.49
$t_{cellCycle}$[h]
p_{div} [h^{-1}]
E'
E''
E'''
E''''
inducer
F'
F''
F'''
F''''
responder